РОССИЙСКИЙ ГОСУДАРСТВЕННЫЙ ПЕДАГОГИЧЕСКИЙ УНИВЕРСИТЕТ им. А. И. ГЕРЦЕНА
HERZEN STATE PEDAGOGICAL UNIVERSITY of RUSSIA

ISSN 2687-153X

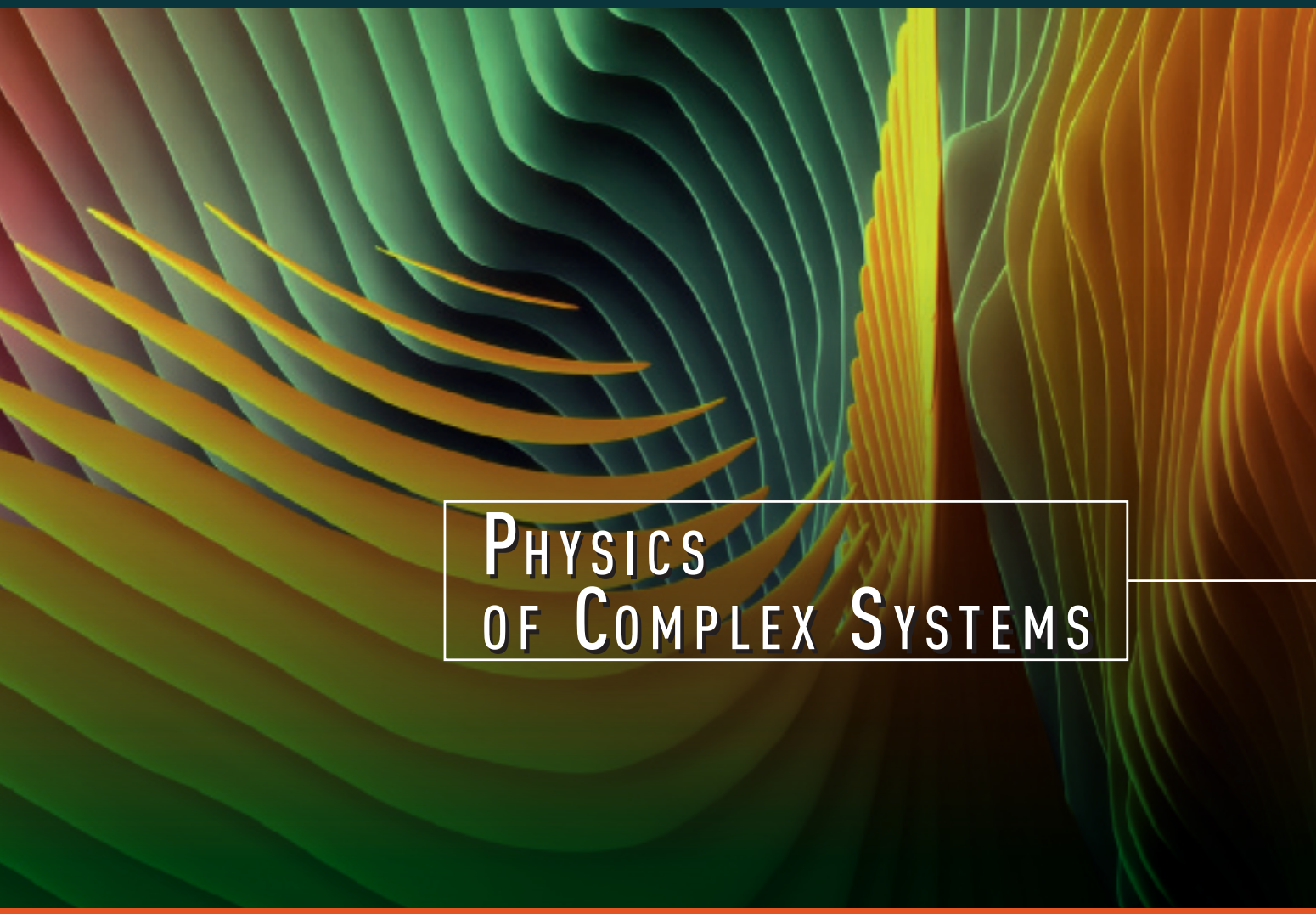

Physics of Complex Systems

Т. 7 № 2 **2026**

Vol. 7 No. 2 **2026**

Herzen State Pedagogical University of Russia

ISSN 2687-153X (online)
physcomsys.ru
https://www.doi.org/10.33910/2687-153X-2026-7-2
2026. Vol. 7, no. 2

PHYSICS OF COMPLEX SYSTEMS

Mass Media Registration Certificate El No. FS77-77889, issued by Roskomnadzor on 10 February 2020
Peer-reviewed journal
Open Access
Published since 2020
4 issues per year

Publishing house of Herzen State Pedagogical University of Russia
48 Moika Emb., Saint Petersburg 191186, Russia
E-mail: izdat@herzen.spb.ru
Phone: +7 (812) 312-17-41

Data size 4,52 Mbyte
Published at 30.06.2026

Editors of the English text *I. A. Nagovitsyna, K. Yu. Rybachuk*
Corrector *N. A. Sinenikolskaya*
Cover design by *O. V. Rudneva*
Layout by *D. V. Romanova*

Saint Petersburg, 2026

CONTENTS

Condensed Matter Physics.
Solid state physics

UDC 538.9

EDN CGGAPH
https://www.doi.org/10.33910/2687-153X-2026-7-2-59-64

Correlations between NMR data, Mössbauer spectroscopy data and the EFG tensor parameters for copper nodes in $RBa_2Cu_3O_{7-x}$ superconducting metal oxides

A. V. Marchenko [1], T. E. Baimirzaeva [1], V. S. Kiselev [1], P. P. Seregin ✉[1]

[1] Herzen State Pedagogical University of Russia, 48 Moika Emb., Saint Petersburg 191186, Russia

Authors

Alla V. Marchenko, ORCID: 0000-0002-9292-2541, e-mail: al7140@rambler.ru

Tamara E. Baimirzaeva, e-mail: toma4535@mail.ru

Valentin S. Kiselev, e-mail: kiselev.valentin@gmail.com

Pavel P. Seregin, ORCID: 0000-0001-5004-2047, e-mail: ppseregin@mail.ru

For citation: Marchenko, A. V., Baimirzaeva, T. E., Kiselev, V. S., Seregin, P. P. (2026) Correlations between NMR data, Mössbauer spectroscopy data and the EFG tensor parameters for copper nodes in $RBa_2Cu_3O_{7-x}$ superconducting metal oxides. *Physics of Complex Systems*, 7 (2), 59–64. https://www.doi.org/10.33910/2687-153X-2026-7-2-59-64 EDN CGGAPH

Received 13 January 2026; reviewed 3 February 2026; accepted 3 February 2026.

Funding: The study had no financial support.

Abstract. Linear ratios have been determined between the quadrupole interaction constants, measured by nuclear magnetic resonance with the ^{63}Cu isotope, emission Mössbauer spectroscopy with the ^{67}Zn isotope and the principal component of the electric field gradient tensor in the copper nodes of $RBa_2Cu_3O_7$ ceramic superconductors. These ratios make it possible to determine compounds in which copper is bivalent without using any models of charge distribution across the nodes within the crystal lattice.

Keywords: nuclear magnetic resonance, Mössbauer spectroscopy, electric field gradient tensor, high-temperature superconductors, electronic defects

Introduction

Determining the spatial distribution of electronic defects in the lattices of superconducting copper metal oxides is one of the urgent problems in the physics of high-temperature superconductivity. This problem can be effectively solved by a comparison of experimentally determined and calculated parameters of the electric field gradient (EFG) tensor for copper nodes.

Nuclear magnetic resonance (NMR) with the ^{63}Cu isotope (Asayama et al. 1996) and emission Mössbauer spectroscopy (EMS) with the ^{67}Cu parent isotope (Bordovsky et al. 2012) are the most applicable methods used to determine the EFG parameters for copper nodes. The measurement results of both methods can be presented as a quadrupole interaction constant

$$C = eQU_{zz} \quad (1)$$

and the EFG tensor asymmetry parameter

$$\eta = (U_{yy} - U_{xx})/U_{zz}, \quad (2)$$

where U_{zz}, U_{yy} and U_{xx} are the diagonalized EFG tensor components on the probe nucleus, $|U_{zz}| \geq |U_{yy}| \geq |U_{xx}|$, and Q is the quadrupole moment of the probe nucleus.

For the $^{63}Cu^{2+}$ probe, EFG on the nuclei is created by the crystalline lattice ions (crystalline EFG) and the non-spherical valence shell of the probe atom (valence EFG). When the orientations of the two tensors' principal axes coincide, then the ratio occurs

$$eQU_{zz} = eQ(1 - \gamma)\, V_{zz} + eQ(1 - R_o)\, W_{zz}, \quad (3)$$

where U_{zz}, V_{zz} and W_{zz} are total, crystalline and valence EFG tensor principal components for the $^{63}Cu^{2+}$ probe, and γ and R_0 are Sternheimer coefficients for the probe.

If EMS with the ^{67}Zn isotope obtained from the ^{67}Cu parent nuclei is used for the experimental determination of the EFG tensor parameters in copper nodes, we should take into account that zinc valence electrons do not contribute to the EFG for the $^{67}Zn^{2+}$ probe, which results in

$$eQU_{zz} \approx eQ(1 - \gamma)V_{zz}. \quad (4)$$

It is of undoubted interest to find the ratios between NMR spectroscopy data with the ^{63}Cu isotope, EMS data with the $^{67}Cu(^{67}Zn)$ isotopes and the crystalline EFG tensor principal components in order to evaluate the charge states of atoms in the superconductive lattices.

In the present work, such ratios are established between the quadrupole interaction constants for the ^{63}Cu (C_{Cu}), ^{67}Zn (C_{Zn}) nuclei and the crystal EFG tensor principal component V_{zz} for the bivalent copper nodes in the $RBa_2Cu_3O_7$ lattices (R = Nd, Sm, Eu, Gd, Y, Er, Tm,Yb), as well as for the monovalent copper nodes in the $YBa_2Cu_3O_6$, Cu_2O and $Nd_{1.85}Ce_{0.15}CuO_4$ lattices, making it possible to evaluate the validity of charge distribution models for crystal lattices of high-temperature superconductors.

Experimental methodology

The $RBa_2Cu_3O_{7-x}$ samples were prepared using the ceramic technology with the ^{67}Cu isotope, obtained by the $^{67}Zn(n, p)^{67}Cu$ reaction irradiating ^{67}ZnO with fast reactor neutrons, followed by the chromatographic detachment of the carrier-free $^{67}CuCl_2$ preparation. The $RBa_2Cu_3O_7$ control samples had a superconducting phase transition temperature within the 75–85 K range and a rhombohedral structure, while the $YBa_2Cu_3O_6$ control samples did not display a transition to the superconducting state up to 4.2 K and had a tetragonal structure.

$Nd_{1.85}Ce_{0.15}CuO_4$ ceramics were synthesized by sintering the corresponding oxides in the air at 1,120 °C, followed by annealing in argon at 900 °C. The ^{67}Cu radioactive isotope was injected into ceramics by diffusion alloying at 900 °C for an hour. The control samples were single-phase, and T_c = 22 K was obtained for the $Nd_{1.85}Ce_{0.15}CuO_4$ ceramics. Copper nitrous oxide was obtained by decomposition of the copper nitrate.

The ^{67}Zn Mössbauer spectra were recorded at 4.2 K with the ^{67}ZnS absorbers (1,000 mG/cm^2).

The ^{63}Cu NMR data for $RBa_2Cu_3O_{7-x}$ were taken from (Matsumura et al. 1998; Pennington et al. 1989; Takatsuka et al. 1991), for Cu_2O from (de Wijn, de Wildt 1966), and for $Nd_{1.85}Ce_{0.15}CuO_4$ from (Kambe et al. 1991).

The crystalline EFG tensors in the copper sites within the $RBa_2Cu_3O_{7-x}$, $YBa_2Cu_3O_6$, $Nd_{1.85}Ce_{0.15}CuO_4$ and Cu_2O lattices were calculated according to the point charges approximation. The $RBa_2Cu_3O_{7-x}$, $YBa_2Cu_3O_6$, $Nd_{1.85}Ce_{0.15}CuO_4$ and Cu_2O lattices were represented as a superposition of sublattices

$$\begin{gathered} RBa_2Cu(l)Cu(2)_2O(l)_2O(2)_2O(3)_2O(4), \\ YBa_2Cu(1)Cu(2)_2O(1)_2O(2)_2O(3)_2, \\ (Nd_{1.85}Ce_{0.15})CuO_4, \\ Cu_4O_2, \end{gathered} \quad (5)$$

and the tensor components for the node were written as the sum of the contributions from the individual sublattices

$$V_{\alpha\alpha} = \sum_k e_k^* \sum_n \frac{1}{r_{ki}^3}\left(3\frac{\alpha_{kn}^2}{r_{kn}^2} - 1\right) = \sum_k e_k^* G_{\alpha\alpha k}\ ,$$

 https://www.doi.org/10.33910/2687-153X-2026-7-2-59-64

$$V_{\alpha\beta} = \sum_k e_k^* \sum_n \frac{3\alpha_{kn}\beta_{kn}}{r_{kn}^5} = \sum_k e_k^* G_{\alpha\beta k} \ , \tag{6}$$

where k is the summation index over the sublattices k = 1 – Y, k = 2 – Ba, k = 3 – Cu1, k = 4 – Cu2, k = 5 – O1, k = 6 – O2, k = 7 – O3, k = 8 – O4, n is the summation index over the sublattice nodes, α, β are the Cartesian coordinates, r_{kn} is the distance from the k_n ion to the lattice site under consideration, and e^*_k is the effective charge of the atoms in the k-sublattice.

To calculate the crystalline EFG tensor for the $RBa_2Cu_3O_7$ series and for $YBa_2Cu_3O_6$, the atom position in the unit cell and the unit cell parameters were used according to (Le Page et al. 1987; Tarascon et al. 1987). While calculating the EFG tensor in the copper nodes of the Cu_2O lattice, the atom coordinates within the unit cell and the unit cell parameters were used from (Wells 1984). For the $Nd_{1.85}Ce_{0.15}CuO_4$ lattice, the atom coordinates in the elementary cell and the lattice constants were used according to (Sadowski et al. 1990).

Results and discussion

Figs. 1 and 2 display experimental data for the values of the quadrupole interaction constant for the ^{63}Cu nuclei in the Cu1 ($|C_{Cu1}|$) and Cu2 ($|C_{Cu2}|$) nodes of the $RBa_2Cu_3O_7$ lattices, as well as in the copper ($|C_{Cu+}|$) nodes of the Cu_2O, $YBa_2Cu_3O_6$ and $Nd_{1.85}Ce_{0.15}CuO_4$ lattices obtained by NMR with the ^{63}Cu [3–12] and EMS with the ^{67}Cu(^{67}Zn) (our original data), in the form of $|C_{Cu1}| = f(C_{Zn})$, $|C_{Cu2}| = f(C_{Zn})$ and $|C_{Cu+}| = f(C_{Zn})$ dependencies.

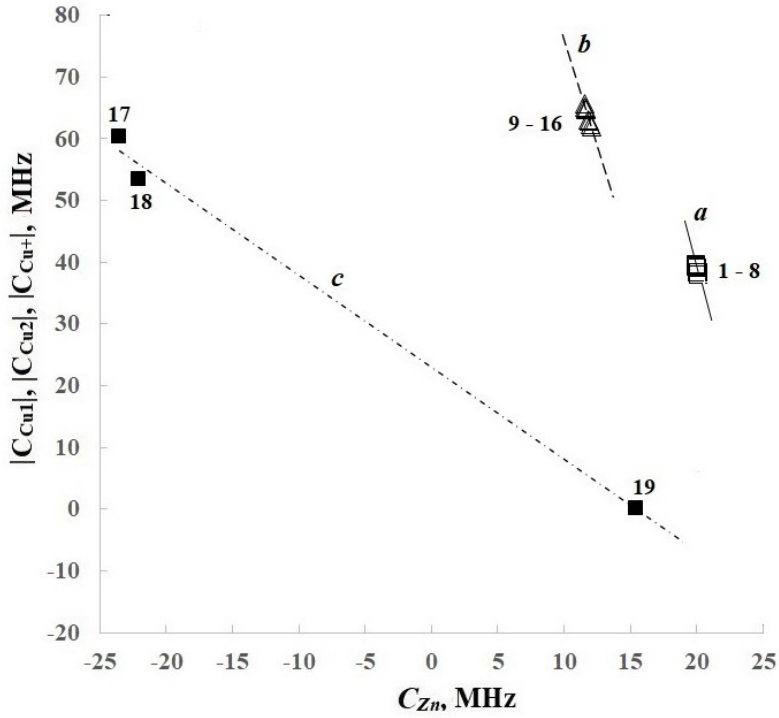

Fig. 1. Experimental dependences $|C_{Cu1}| = f(C_{Zn})$, $|C_{Cu2}| = f(C_{Zn})$ and $|C_{Cu+}| = f(C_{Zn})$. The $|C_{Cu1}|$, $|C_{Cu2}|$ and $|C_{Cu}|$ data were obtained by NMR with the ^{63}Cu [3–12], and the C_{Zn} data were obtained by EMC with the ^{67}Cu(^{67}Zn). Here $|C_{Cu1}|$, $|C_{Cu2}|$ and $|C_{Cu+}|$ are the quadrupole interaction constants for the ^{63}Cu centers in copper nodes, and C_{Zn} are the quadrupole interaction constants for the ^{67}Zn centers in copper nodes. Designations: Cu1 in $NdBa_2Cu_3O_7$ (1), $SmBa_2Cu_3O_7$ (2), $EuBa_2Cu_3O_7$ (3), $YBa_2Cu_3O_7$ (4), $GdBa_2Cu_3O_7$ (5), $ErBa_2Cu_3O_7$ (6), $TmBa_2Cu3O_7$ (7), $YbBa_2Cu_3O_7$ (8), $NdBa_2Cu_3O_7$ (9), $SmBa_2Cu_3O_7$ (10), $EuBa_2Cu_3O_7$ (11), $YBa_2Cu_3O_7$ (12), $GdBa_2Cu_3O_7$ (13), $ErBa_2Cu_3O_7$ (14), $TmBa_2Cu_3O_7$ (15), $YbBa_2Cu_3O_7$ (16), Cu1 in $YBa_2Cu_3O_6$, (17) Cu in Cu_2O (18) and Cu in $Nd_{1.85}Ce_{0.15}CuO_4$ (19)

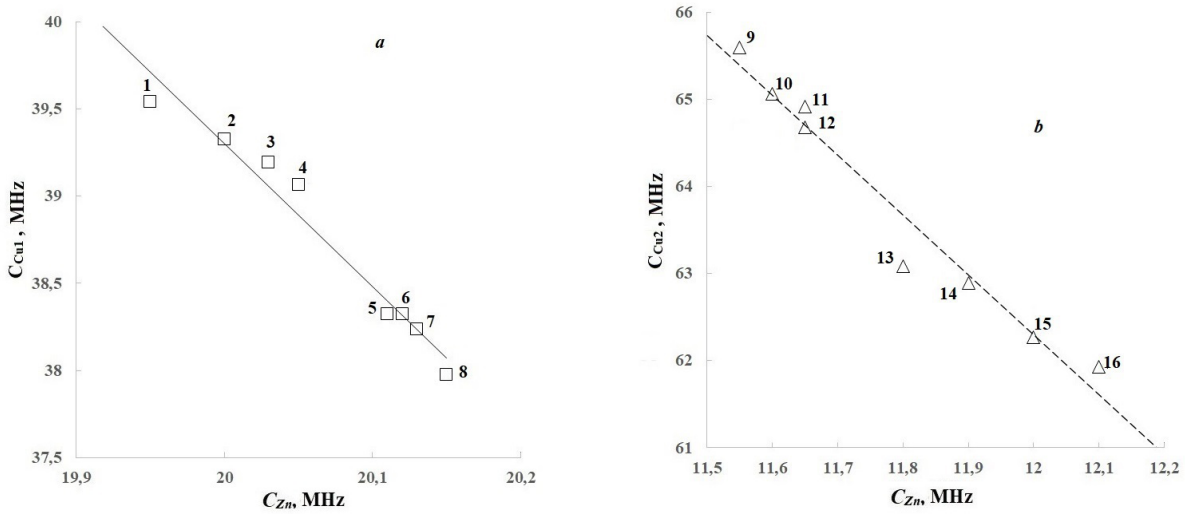

Fig. 2. Experimental dependencies $|C_{Cu1}| = f(C_{Zn})$ (*a*) and $|C_{Cu2}| = f(C_{Zn})$ (*b*) in an enlarged scale

It can be seen that the data corresponding to the bivalent copper compounds are located on two different linear dependences corresponding to the Cu1 and Cu2 centers,

$$|C_{Cu1}| = -8.21\ C_{Zn} + 203.6, \tag{7}$$

$$|C_{Cu2}| = -9.93\ C_{Zn} + 181.2, \tag{8}$$

and what is more is that these dependences differ from the dependence obtained for the Cu+ single-phase copper centers

$$|C_{Cu+}| = -1.49\ C_{Zn} + 23, \tag{9}$$

which is characterized by an insignificant contribution to the EFG for the ^{63}Cu nuclei from the valence electrons (all values in (7–9) are indicated in MHz).

It should also be concluded that the contribution from the valence electrons to the total EFG for the ^{63}Cu nuclei is the same for both Cu1 [$eQ(1 - R)W_{zz} \sim 204$ MHz] and Cu2 [$eQ(1 - R)W_{zz} \sim 145$ MHz] centers in all the studied compounds. At the same time, a decrease in $|C_{Cu1}|$ and $|C_{Cu2}|$ with an increase in C_{Zn} is evidence for the opposite signs of the valence and crystalline contributions in formula (1) and leads to the ratio

$$|(1 - R)W_{zz}| > |(1 - \gamma)V_{zz}| \tag{10}$$

for bivalent copper centers in $RBa_2Cu_3O_7$.

The dependences $|C_{Cu1}| = f(C_{Zn})$ and $|C_{Cu2}| = f(C_{Zn})$ and ratios (7, 8) can be used to select the compounds in which copper is bivalent and for which the directions of the principal axes of the valence and crystalline EFG tensors coincide. Such a selection does not use any models of charge distribution along the nodes of the crystal lattice.

Fig. 3 and Fig. 4 shows the dependences $|C_{Cu1}| = f(V_{zz})$ and $|C_{Cu2}| = f(V_{zz})$, which are similar to the dependences $|C_{Cu1}| = f(C_{Zn})$ and $|C_{Cu2}| = f(C_{Zn})$ since C_{Zn}, according to (2), is proportional to V_{zz}. When calculating V_{zz}, the choice of a model of charge distribution across the lattice sites is of fundamental importance. The best agreement with the experiment is shown by models

$$\mathbf{R^{3+}Ba_2^{1.98+}Cu(1)_2^{2.04+}Cu(2)_2^{2.1+}O(1)_2^{2.06-}O(2)_2^{1.99-}O(3)_2^{1.88-}O(4)^{1.32-}} \tag{11}$$

$$\mathbf{Nd_{1.85}^{3.075+}Ce_{1.85}^{3.075+}Cu^{1.85+}O_4^{2-}} \tag{12}$$

$$\mathbf{Y^{3+}Ba_2^{2+}Cu(1)_2^{2+}Cu(2)_2^{2+}O(1)_2^{2-}O(2)_2^{2-}O(3)_2^{2-}} \tag{13}$$

$$\mathbf{Cu_4^{+}O_2^{2-}}. \tag{14}$$

 https://www.doi.org/10.33910/2687-153X-2026-7-2-59-64

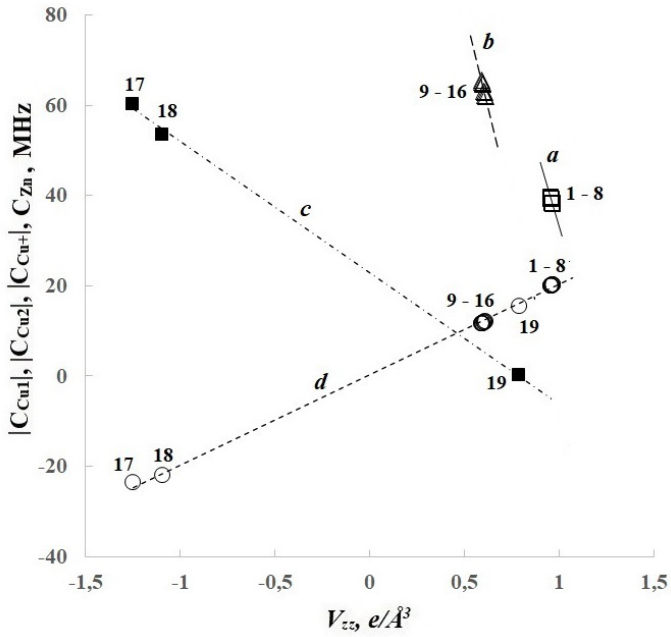

Fig. 3. Experimental dependences $|C_{Cu1}| = f(V_{zz})$, $|C_{Cu2}| = f(V_{zz})$, $|C_{Cu+}| = f(V_{zz})$ and $C_{Zn} = f(V_{zz})$. The $|C_{Cu1}|$ and $|C_{Cu2}|$ data were obtained by NMR with the ^{63}Cu [3–12], and the C_{Zn} data, by EMS with the ^{67}Cu(^{67}Zn). Here V_{zz} is the crystalline EFG tensor principal component

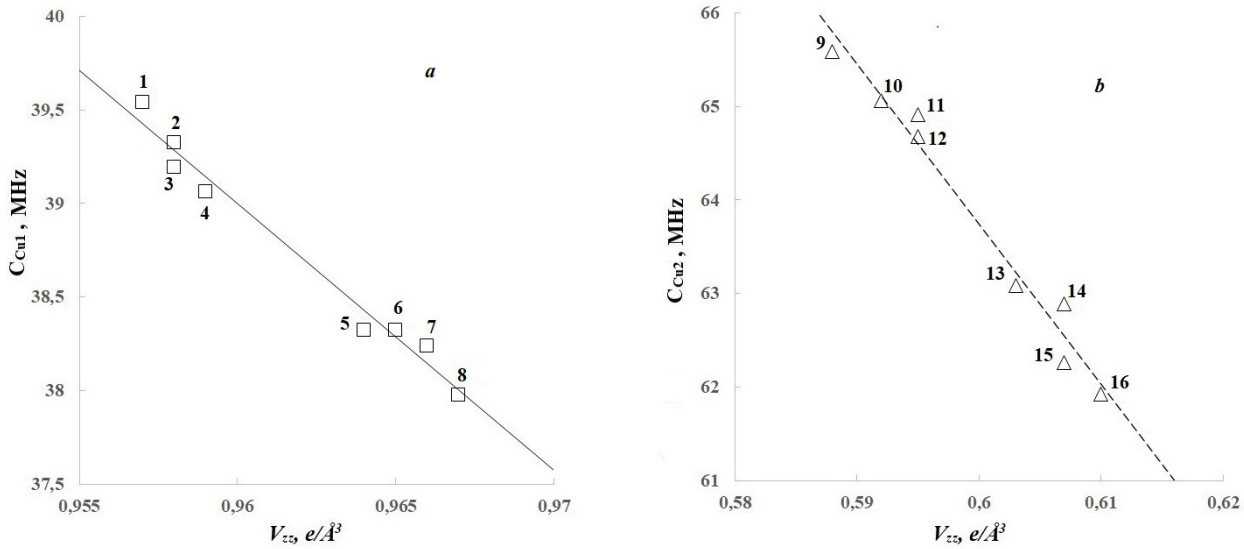

Fig. 4. Experimental dependences $|C_{Cu1}| = f(V_{zz})$ (*a*) and $|C_{Cu2}| = f(V_{zz})$ (*b*) in an enlarged scale

It can be seen that the data corresponding to the bivalent copper compounds are still located on two linear dependences corresponding to Cu1 and Cu2

$$|CCu1| = -142.5V_{zz} + 175.8, \tag{15}$$

$$|CCu2| = -176.1V_{zz} + 170, \tag{16}$$

and once more these dependences differ from the dependence obtained for Cu+ monovalent copper centers by a small contribution to the total EFG on ^{63}Cu nuclei

$$|CCu+| = -29.1V_{zz} + 23. \tag{17}$$

This difference is especially noticeable in the case of the bivalent zinc centers, for which the contribution to the total EFG from valence electrons, firstly, coincides in sign with the crystalline EFG, and, secondly, the contribution from valence electrons is very small

$$C_{Zn} = 20V_{zz} + 0.24. \quad (18)$$

In formulas (15–18), the values of $|C_{Cu1}|$, $|C_{Cu2}|$, $|C_{Cu+}|$ and C_{Zn} are given in MHz, and the values of V_{zz} are in e/Å^3.

The ratios (15, 16) can be used to evaluate the reliability of the proposed model charge distributions within the lattice sites for superconductive ceramics.

Conclusion

Thus, linear dependences between $|C_{Cu}|$ (NMR data with the ^{63}Cu) and C_{Zn} (EMS data with the ^{67}Cu(^{67}Zn)) for bivalent copper metal oxides are demonstrated, which indicates the similarity of the copper electronic structure in these lattices. A similar linear dependence is found between $|C_{Cu}|$ (NMR data with the ^{63}Cu) and V_{zz} (calculated in the point charge model approximation), which can be used to evaluate the reliability of the proposed model charge distributions within the lattice sites for superconductive ceramics.

Conflict of Interest

The authors declare that there is no conflict of interest, either existing or potential.

Author Contributions

The authors have made an equal contribution to the preparation of the paper.

References

Asayama, K., Kitaoka, Y., Zheng, G.-Q., Ishida, K. (1996) NMR studies of high T_c superconductors. *Progress in Nuclear Magnetic Resonance Spectroscopy*, 28 (3–4), 221–253. https://doi.org/10.1016/0079-6565(95)01025-4 (In English)

Bordovsky, G. A., Seregin, P. P., Marchenko, A. V. (2012) *Mössbauer of negative U centers in semiconductors and superconductors. Identification, properties, and application*. Saarbrücken: LAP LAMBERT Academic Publ., 508 p. (In English)

De Wijn, H. W., de Wildt, J. L. (1966) Temperature dependence of nuclear quadrupole resonance in cuprous oxide. *Physical Review*, 150 (1), 200–201. https://doi.org/10.1103/PhysRev.150.200 (In English)

Kambe, S., Yasuoka, H., Takagi, H. et al. (1991) ^{63,65}Cu-NMR study of oxidized and reduced $Nd_{2-x}Ce_xCuO_4$. *Journal of the Physical Society of Japan*, 60 (2), 400–403. https://doi.org/10.1143/JPSJ.60.400 (In English)

Le Page, Y., Siegrist, T., Sunshine, S. A. et al. (1987) Structural properties of $Ba_2RCu_3O_7$ high-T_c superconductors. *Physical Review B*, 36 (7), 3617–3621. https://doi.org/10.1103/PhysRevB.36.3617 (In English)

Matsumura, M., Shiohara, T., Yamagata, H. (1998) Cu-NQR study in the paramagnetic state in $YBa_2Cu_3O_6$. *Journal of the Physical Society of Japan*, 67 (9), 3267–3274. (In English)

Pennington, C. H., Durand, D. J., Slichter, C. P. et al. (1989) Static and dynamic Cu NMR tensors of $YBa_2Cu_3O_{7-\delta}$. *Physical Review B*, 39 (4), 2902–2905. https://doi.org/10.1103/PhysRevB.39.2902 (In English)

Sadowski, W., Walker, E., Francois, M. et al. (1990) Growth of single crystals, thermal dependency of lattice parameters and Raman scattering in the $Nd_{2-x}Ce_xCuO_4$ system. *Physica C: Superconductivity*, 170 (1-2), 103–111. (In English)

Takatsuka, T., Kumagai, K., Nakajima, H., Yamanaka, A. (1991) Hyperfine fields and quadrupole frequencies at each Cu site in $RBa_2Cu_3O_6$ and $RBa_2Cu_3O_7$ (R: rare-earth element). *Physica C: Superconductivity*, 185–189 (2), 1071–1072. (In English)

Tarascon, J. M., McKinnon, W. R., Greene, L. H. et al. (1987) Oxygen and rare-earth doping of the 90-K superconducting perovskite $YBa_2Cu_3O_{7-x}$. *Physical Review B*, 36 (1), 226–234. https://doi.org/10.1103/PhysRevB.36.226 (In English)

Wells, A. F. (1984) *Structural Inorganic Chemistry*. 5th ed. Oxford: Oxford University Press, 1382 p. (In English)

Condensed Matter Physics.
Functional materials in electronics

UDC 537.226.4+538.911

EDN JCWNAV
https://www.doi.org/10.33910/2687-153X-2026-7-2-65-73

Imprint in spherulitic thin films of lead zirconate titanate

V. P. Pronin ✉[1], A. N. Krushelnitckii [1], A. R. Mazgutova [2], E. Yu. Kaptelov [2], V. S. Senkevich [1, 2], I. P. Pronin [2], S. A. Nemov [3]

[1] Herzen State Pedagogical University of Russia, 48 Moika Emb., Saint Petersburg 191186, Russia
[2] Ioffe Institute, 26 Polytechnicheskaya Str., Saint Petersburg 194021, Russia
[3] Peter the Great St. Petersburg State Polytechnical University, 29B Politekhnicheskaya Str., Saint Petersburg 195251, Russia

Authors

Vladimir P. Pronin, ORCID: 0000-0003-0997-1113, e-mail: pronin.v.p@yandex.ru

Artemii N. Krushelnitckii, ORCID: 0000-0003-3543-8531, e-mail: akrushelnitckii@herzen.spb.ru

Alsu R. Mazgutova, ORCID: 0000-0002-8826-8938, e-mail: valeevaar@mail.ioffe.ru

Evgeny Yu. Kaptelov, e-mail: kaptelov@mail.ioffe.ru

Stanislav V. Senkevich, ORCID: 0000-0002-4503-1412, e-mail: senkevichSV@mail.ioffe.ru

Igor P. Pronin, ORCID: 0000-0003-3749-8706, e-mail: petrovich@mail.ioffe.ru

Sergei A. Nemov, ORCID: 0000-0003-3749-8706, e-mail: nemov_s@mail.ru

For citation: Pronin, V. P., Krushelnitckii, A. N., Mazgutova, A. R., Kaptelov, E. Yu., Senkevich, V. S., Pronin, I. P., Nemov, S. A. (2026) Imprint in spherulitic thin films of lead zirconate titanate. *Physics of Complex Systems*, 7 (2), 65–73. https://www.doi.org/10.33910/2687-153X-2026-7-2-65-73 EDN JCWNAV

Received 13 January 2026; reviewed 3 February 2026; accepted 3 February 2026.

Funding: This work was supported by an internal grant from Herzen State Pedagogical University of Russia, VN-84.

Abstract. The reported study investigates the influence of microstructure (geometric dimensions of spherulitic blocks), external field amplitude, and aging on the magnitude of the internal field (imprint) in thin lead zirconate titanate films formed by a two-stage RF magnetron sputtering on a platinized silicon substrate. It is shown that the increase in the internal field during aging occurs as a result of the upward diffusion of oxygen vacancies (the Gorsky effect), caused by bending stresses in the thin film. It is hypothesized that the source of oxygen vacancies in the perovskite lattice is the additional oxidation of excess lead oxide located at the interfaces and in the intercrystalline space of the thin films.

Keywords: thin PZT films, RF magnetron sputtering, spherulitic microstructure, imprint, self-polarization, oxygen vacancies

Introduction

Imprint refers to the presence of an internal (built-in) electric field in a thin ferroelectric film, often described as a voltage shift. This shift manifests as a displacement of dielectric hysteresis loops (P-V curves) or capacitance-voltage (C-V) characteristics along the abscissa axis (Alexe et al. 2001; Hiboux, Muralt 2001; Lee, Ramesh 1996; Okamura et al. 1999; Sun et al. 1999; Warren et al. 1995). When ferroelectric films are used in non-destructive memory elements, the presence of such a field is an undesirable (parasitic) phenomenon, because switching the ferroelectric polarization in a planar thin-film ferroelectric capacitor requires the application of an external field of varying magnitude. In other words, a strong internal field may render the external (switching) field insufficient to reorient the polarization opposite to the internal field, leading to memory element failure.

Imprint is associated with the appearance of a self-polarized state (macroscopic polarization) in freshly prepared films, a phenomenon referred to as self-polarization since the early 1990s (Frey et al.

2001; Kholkin et al. 1998; Sviridov et al. 1994; Takayama et al. 1991). In the Russian literature, another term 'natural unipolarity' or simply 'unipolarity' is often used (Gavrilyachenko et al. 1968; Kanareikin et al. 2016). It has been shown that the presence of a strong internal field and self-polarization are distinct advantages when thin films are used in microelectromechanical systems (MEMS) and related applications where polarization switching is not required (Akkopru-Akgun, Trolier-McKinstry 2023; Akkopru-Akgun et al. 2019; Araujo et al. 2016; Shvartsman et al. 2005; Song et al. 2021). This is due, on the one hand, to the elimination of the costly process of pre-polarizing the thin film and, on the other hand, to the increased stability of the polar state under external (mechanical, electrical, thermal) influences.

An analysis of previous studies on the nature of the internal field and macroscopic polarization reduces to the action of two relatively distinct physical mechanisms:

— a mechanical stress gradient across the film thickness,

— a collective polarizing effect of charges or potentials present in the thin film.

In the first case, the mechanism in question is the mechanoelectric effect (Bursian et al. 1969; Sviridov et al. 1994), later termed the flexoelectric effect (Gruverman et al. 2003; Yudin, Tagantsev 2013), which reduces to the appearance of opposite-sign charges in a thin-film ferroelectric capacitor under mechanical bending (Bursian et al. 1969). The presence of a mechanical stress gradient can induce macroscopic polarization even in nonpolar materials (Ehre et al. 2007).

In the second case, the mechanism of internal field formation and self-polarization is associated with:

— the action of a space charge at either the bottom or top interface of a thin-film ferroelectric capacitor (Frey et al. 2001; Kholkin et al. 1998; Sun et al. 1999),

— a non-uniform charge distribution across the thickness of the thin film or charge diffusion (Hiboux, Muralt 2001),

— the presence of ordered dipoles formed by charged defects or impurities (Okamura et al. 1999).

The use of electrodes made from different materials also gives rise to an internal field due to the difference in Schottky barrier heights at the thin film-electrode interface (Choi et al. 1997). The role of surface charge, which can also lead to self-polarization, is noted in (Shen et al. 2024; Stephanovich et al. 2023).

Thus, even from the above brief account of the causes (or mechanisms) of imprint formation, it is clear that a definitive explanation of the nature of this phenomenon has yet to be developed. At the same time, there is clear practical interest in this class of thin films, particularly lead zirconate titanate (PZT) solid solutions, due to their considerable potential for use in MEMS devices (Akkopru-Akgun, Trolier-McKinstry 2023; Akkopru-Akgun et al. 2019; Li, Feng 2025; Liu et al. 2024; Song et al. 2021). The aim of this study was to investigate imprint in PZT thin films, whose composition corresponds to the morphotropic phase boundary (MPB) region, characterized by a spherulitic microstructure and block size, under the influence of strong alternating fields and during long-term aging.

Materials and methods

Thin films of a composition corresponding to the morphotropic phase boundary region on the rhombohedral phase side, with the elemental ratio Zr/Ti = 54/46, were prepared by a two-stage method of RF magnetron sputtering on platinized silicon ($Pt/Ti/SiO_2/Si$) substrates. The films were deposited at different target-substrate distances (D = 30–70 mm) and then annealed at 580 °C in air. The film thickness was ~ 500 nm. A detailed description of the sample preparation is given in (Staritsyn et al. 2023a). To exclude the effect of differences in electrode material, the top electrodes were also made of platinum.

Microstructure studies of the samples were conducted using scanning electron microscopy (SEM, EVO-40, Zeiss). Phase analysis was performed using X-ray diffraction (DRON-7) and optical microscopy (Nikon Eclipse LV150). Dielectric properties were studied with an E7-30 immittance meter and a modified Sawyer-Tower circuit.

Results and discussion

The features of the spherulitic microstructure are associated with the crystallization behaviour of the perovskite phase, which involves the nucleation, growth, and subsequent merging of individual, nearly round islands during high-temperature annealing of pre-deposited amorphous thin PZT films, ultimately forming a single-phase block structure (Staritsyn et al. 2023a), Fig. 1. The linear size of the blocks in the studied films depended on the deposition conditions and decreased from 35–40 μm (at D = 30 mm, Fig. 1a) to 10–15 μm (in films deposited at D = 60–70 mm, Fig. 1c).

 https://www.doi.org/10.33910/2687-153X-2026-7-2-65-73

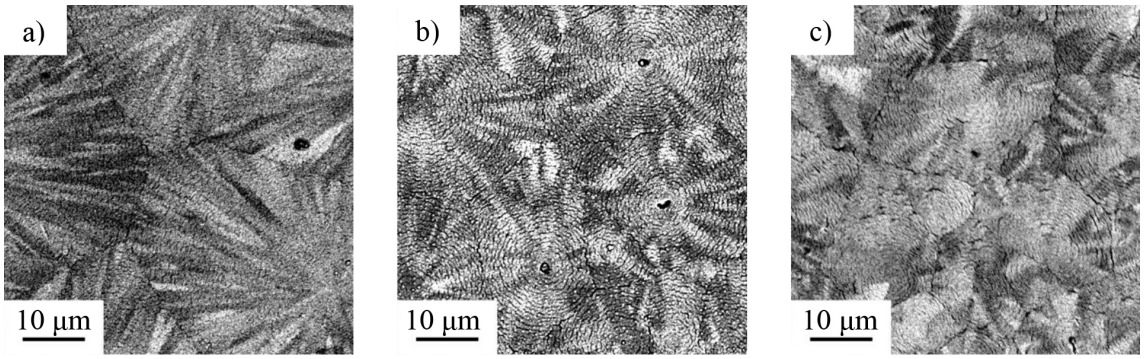

Fig. 1. SEM images of thin PZT films deposited at target-substrate distances D = 30 mm (a), D = 40 mm (b), and D = 60 mm (c)

The dielectric hysteresis loops (P-V) measured on as-prepared films (the holding time did not exceed several days) revealed the presence of an internal field: the P-V curves were shifted along the abscissa axis toward negative voltages (Fig. 2a-c). This means that the field vector was oriented from the free surface toward the bottom interface of the film. In weak external fields (E_{ext} = 200 kV/cm), the internal field (E_{int}) ranged from ~10 to 30 kV/cm. Applying a strong field to the samples resulted in a significant decrease in E_{int}, i. e., in symmetrization of the hysteresis loops (Fig. 2a-c). Moreover, under strong fields (E_{ext} = 600 kV/cm), a sign reversal of the field was observed in the films, Fig. 3a and Fig. 4a. The highest value of E_{int} with reverse orientation exceeded 10 kV/cm in the film deposited at D = 40 mm.

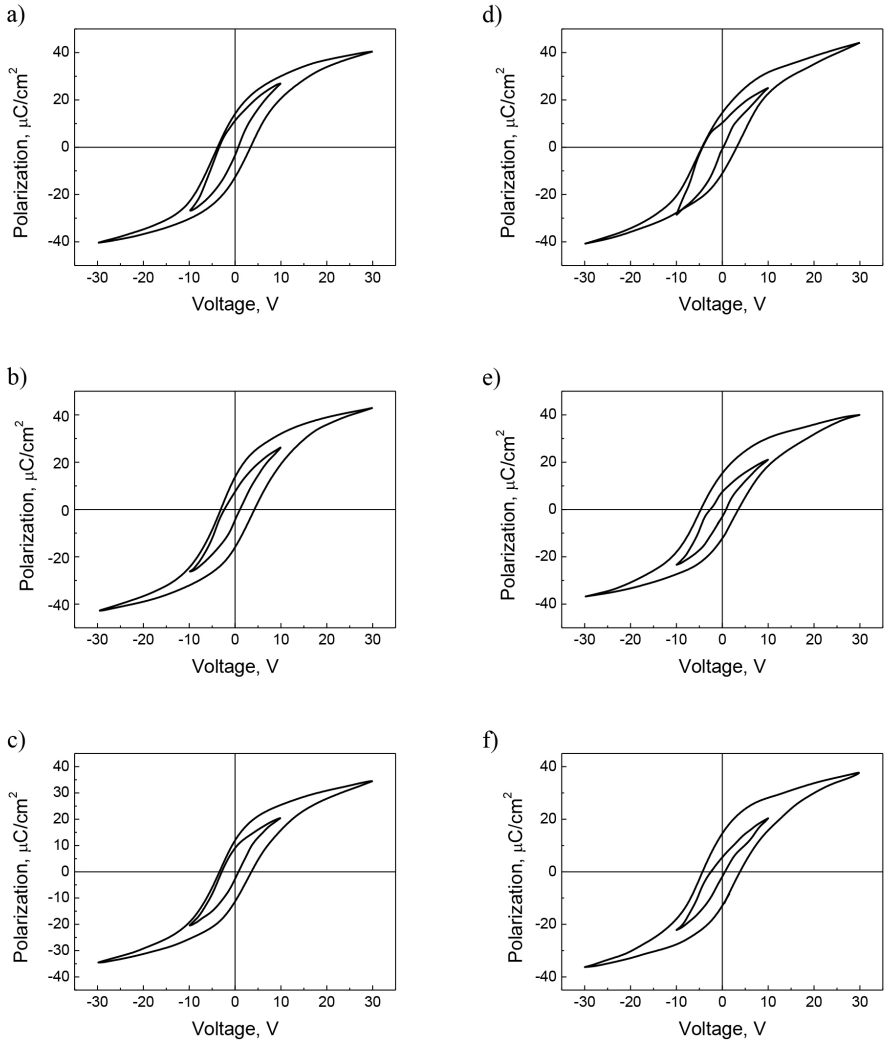

Fig. 2. P-V loops of as-prepared films (a–c) and after aging for 8*10⁷ s (d–f), deposited at different target-substrate distances: D = 30 mm (a, d), D = 40 mm (b, e) and D = 60 mm (c, f)

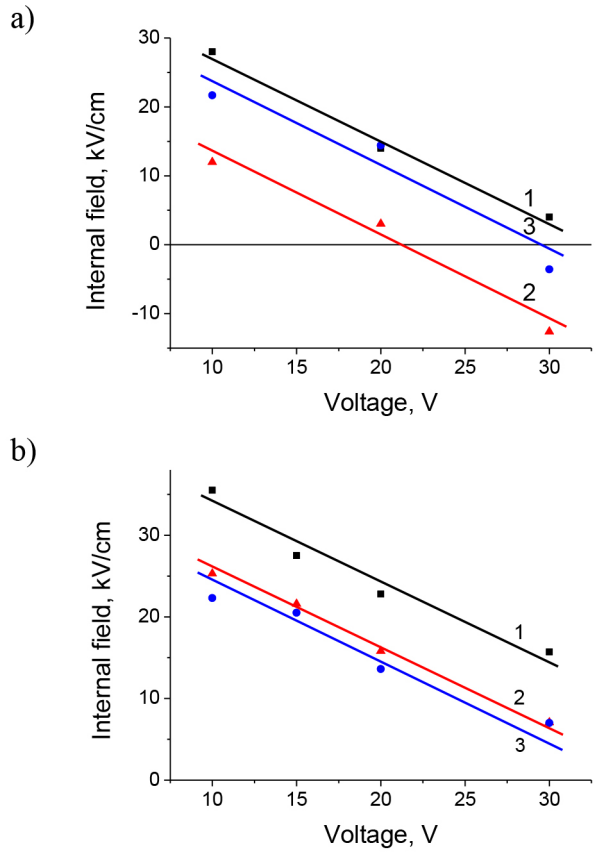

Fig. 3. Internal field calculated from the P-V loops of as-prepared PZT films (a) and after aging for $8*10^7$ s (b), deposited at different target-substrate distances: curves 1 — D = 30 mm, 2 — D = 40 mm, 3 — D = 60 mm

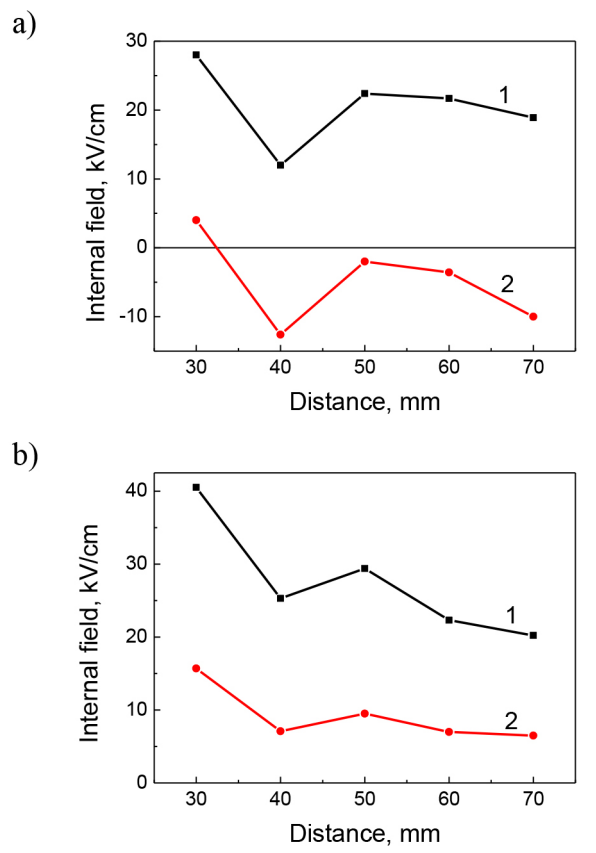

Fig. 4. The internal field calculated from the hysteresis loops of as-prepared PZT films (a) and after aging $8*10^7$ s (b) when applying a weak (200 kV/cm, curve 1) and strong (600 kV/cm, curve 2) electric field

A significant change in the shift of the P-V loops along the abscissa axis was observed after aging the films for $8*10^7$ s. From Figs. 2d-f and Figs. 3b and 4b, it is evident that an increase in the magnitude of the internal field directed from the free surface of the films to the bottom interface was observed in all the samples, and the field orientation persisted even under the application of strong fields. In weak fields, the value of E_{int} exceeded 20–25 kV/cm, and the highest value (~40 kV/cm) was achieved in the film deposited at D = 30 mm. Under the application of strong fields, the orientation of the internal field vector was maintained in all the studied samples.

The observed changes in the dielectric hysteresis loops allow us to make several assumptions regarding the mechanisms of internal field (and self-polarization) formation in thin PZT films, based on the contribution of internal charges (electrons and charged oxygen vacancies) to the effect, as well as on the features of the spherulitic microstructure and the associated bending mechanical stresses.

The appearance of the internal field in as-prepared films is attributed to the presence of charged oxygen vacancies (and electrons), whose high concentration results from the presence of excess lead oxide. Measurements of the lead content in the formed perovskite films by energy dispersive x-ray spectroscopy showed an excess of 6–9 mol.%. It is assumed that at room temperature, the equilibrium state of lead oxide is realized in the form of lead dioxide (PbO_2) (Tentilova et al. 2012), and further oxidation of lead to the tetravalent state occurs through the capture of mobile oxygen atoms from the perovskite lattice and the formation of internal point defects — oxygen vacancies. According to various sources, the activation energy of the pair consisting of two electrons and a doubly positively charged oxygen vacancy varies in the range of ~ 0.1–0.4 eV (Scott 1998). Thus, calculations show that at an activation energy of E_{ac} = 0.22 eV, the concentration of charged oxygen vacancies is ~ 1% of the total oxygen vacancy concentration in a thin PZT film (Valeeva et al. 2022).

According to the data of (Pronin et al. 2002), in the absence of a top electrode, the formation of a negative space charge during the growth of a PZT thin film occurs through the capture of mobile electrons

 https://www.doi.org/10.33910/2687-153X-2026-7-2-65-73

in deep traps near the bottom thin film-electrode interface. The resulting space charge field can lead to a reorientation of ferroelectric dipoles in the lower part of the thin film or throughout the entire volume in (symmetrically allowed) directions that are as close as possible to the direction of the internal field, and the formation of a unipolar (self-polarized) state, depending on the particular electron concentration (Pronin et al. 2002). It should be noted that, during subsequent deposition of the top contact pads, high-temperature annealing of such unipolar films to the Curie temperature or above leads to a redistribution of electrons between the top and bottom interfaces, the formation of local space charges and internal fields oriented in opposite directions and, thus, to the cancellation of the measured internal field and symmetrization of the hysteresis loops (Okamura et al. 1999; Pronin et al. 2002).

An important aspect here is the distribution of charged oxygen vacancies across the thickness of the thin films. It can be assumed that excess lead is located both at the interfaces of the thin film and in the intercrystallite space. If we assume that a significant portion of the excess lead lies near the bottom interface of the film due to the specific crystallization and growth of spherulitic islands (Pronin et al. 2002), then the generation of oxygen vacancies will occur in the bottom part of the film, and, accordingly, the distribution of vacancies will be uneven and shifted towards the lower interface. The distribution of localized negative charge and the distribution of charged oxygen vacancies is shown schematically in Fig. 5a, which reflects the magnitude of the internal field in freshly prepared films under a weak external field and corresponds to the values of E_{int} on curve 1, Fig. 4a. Apparently, the distribution of excess lead in the thin film in our case is associated with the features of perovskite phase crystallization (changes in spherulitic block size) with variations in the target-substrate distance.

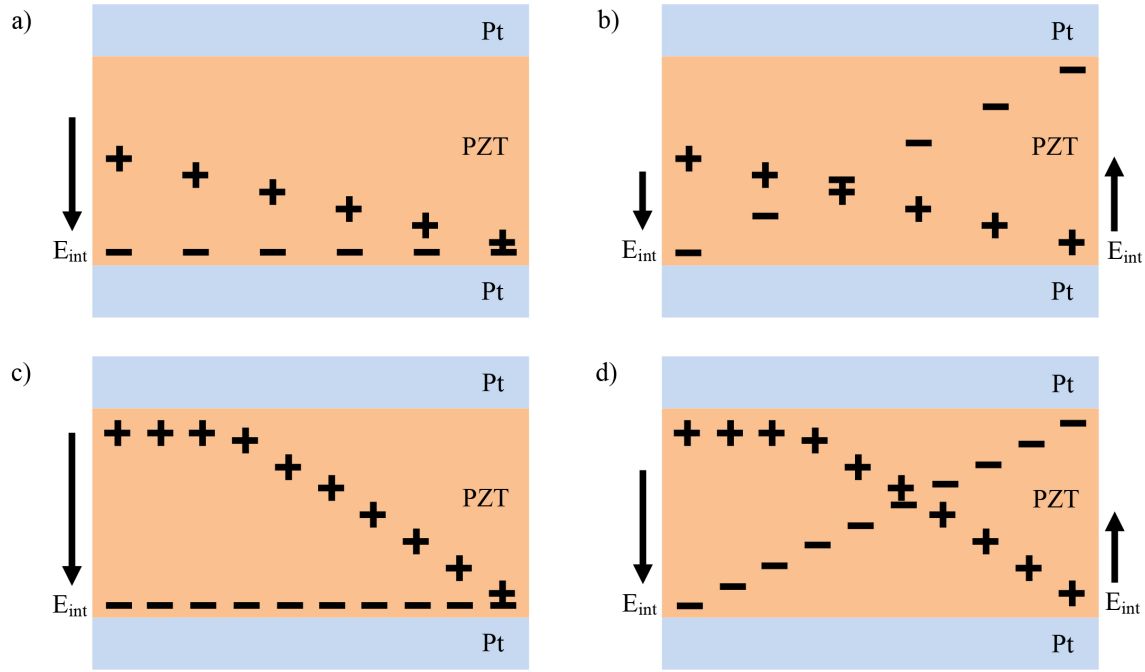

Fig. 5. Distribution of negative charge and charged oxygen vacancies across the thickness of the PZT-film: in a freshly prepared film (a), in a freshly prepared film after application of a strong external field (b), in a film after long-term aging (c) and in a film after long-term aging followed by application of a strong external field (d)

It is assumed that the application of a strong external field leads to the release of electrons from deep traps at the bottom interface and, to a first approximation, to their uniform distribution within the bulk of the thin film. This may result not only in the symmetrization of the hysteresis loops, as is often observed in experiments (Okamura et al. 1999; Pronin et al. 2002; Valeeva et al. 2022), but also in the appearance of an internal field of reverse polarity if charged oxygen vacancies are concentrated in the bottom part of the film, Fig. 5b. Thus, it can be assumed that the appearance of an internal field (imprint) of reverse polarity — oriented toward the free surface of the film — is determined by the nonuniform distribution of positively charged oxygen vacancies.

Obviously, during aging, the concentration of oxygen vacancies should equalize through diffusion, i. e., vacancy diffusion toward the top interface of the film. However, a more probable scenario

is the mechanism of oxygen vacancy diffusion known in the literature as the ascending diffusion effect or the Gorsky effect. The essence of this effect is related to bending deformation of the thin film and the diffusion of large impurity atoms (or defects) in the direction of the mechanical stress gradient, leading to a nonuniform distribution of these atoms across the film thickness (Gorsky 1935). Subsequently, the concept of the Gorsky effect was extended not only to the diffusion of impurity atoms but also to intrinsic point defects, including oxygen vacancies, whose diffusion occurs in the direction opposite to the mechanical stress gradient, Fig. 6 (Kosevich 1975).

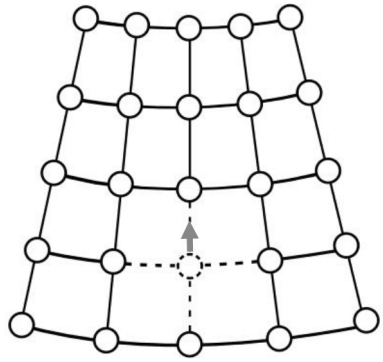

Fig. 6. Oxygen vacancy diffusion in a deformed crystal lattice

In our case, bending of the PZT film–Si substrate system can be caused by at least two factors:
— a difference in the linear thermal expansion coefficients of the film and the substrate,
— crystallization of the perovskite phase from the amorphous phase during high-temperature annealing, accompanied by a change (or more precisely, an increase) in film density, which leads to the appearance of tensile mechanical stresses acting on the perovskite islands from the intermediate pyrochlore phase, Fig. 7a.

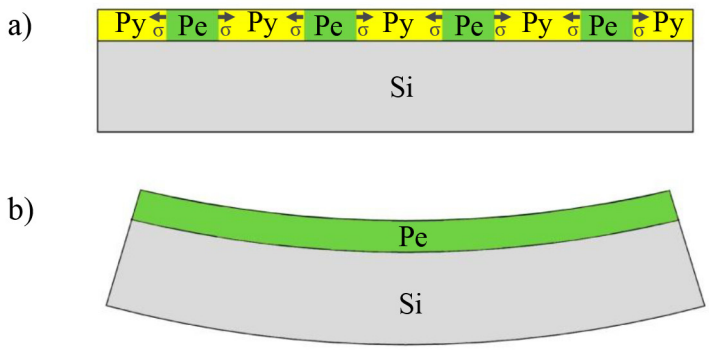

Fig. 7. Perovskite phase crystallization from the amorphous phase during high-temperature annealing (a) and bending deformation of the bimorphic PZT film–Si substrate structure after completion of the perovskite phase crystallization (b)

In PZT films whose composition corresponds to the MPB region, the bending strain in the first case was estimated to be no more than 0.1%, and in the second case, ~ 0.5% (Staritsyn et al. 2023b). Both effects lead to deformation of the bimorphic PZT film–Si substrate structure with a bend towards the free surface of the thin film, Fig. 7b. The presence of bending strain, manifested as a rotation of the crystal lattice of the PZT film and recorded by electron backscatter diffraction, allowed us in our previous work (Valeeva et al. 2025) to estimate the main parameters of the directed diffusion flux of oxygen vacancies in the perovskite lattice, as well as the time required for their diffusion to the top interface, which is ~ 10^7 s, that is, on the order of three months (Fig. 7).

The result of film aging is shown schematically in Fig. 5c. However, to explain the increase in the internal field in aged films, it can be assumed that it is caused not only by the directed diffusion of oxygen vacancies but also by their additional generation, leading both to an increase in the negative space charge

 https://www.doi.org/10.33910/2687-153X-2026-7-2-65-73

localized near the bottom interface of the thin film and the accumulation of positive charges near the top interface of the film. In this case, application of a strong external field no longer leads to a change in the orientation of the internal field (Fig. 5d).

The minimum value of E_{int} at D = 40 mm in Fig. 4 deserves special mention. It was previously shown that in such a film, the maximum angles of crystal lattice rotation in spherulitic blocks and the maximum values of the projection of polarization lying in the plane of the thin film (lateral polarization) were observed, which was caused by the maximum lateral stresses among all films (Staritsyn et al. 2023c). In this case, the reasons for the appearance of maximum lateral polarization values were associated with the redistribution of negative space charge towards the periphery, where, along with the region of deep traps near the bottom interface, the formation of deep traps and space charge occurred at the pyrochlore-perovskite phase boundary throughout the thickness of the PZT film (Senkevich et al. 2024).

Conclusions

This paper investigates the imprint (internal field) phenomenon in PZT thin films with different linear dimensions of spherulitic blocks, obtained by a two-stage RF magnetron sputtering with varying target-to-substrate distances and, consequently, block sizes. It was experimentally demonstrated that:

— in as-prepared films, applying a strong external field (600 kV/cm) leads to a change in the sign of the internal field (imprint);
— as a result of prolonged aging, the internal field magnitude increases significantly;
— the linear dimensions of the spherulitic blocks significantly influence the imprint magnitude.

To explain the observed phenomena, a model is proposed according to which the imprint is the result of the combined effect of a negative space charge, localized primarily in deep traps in the bottom interface region of the thin film, and the positive charge of oxygen vacancies, distributed nonuniformly across the film thickness. It is assumed that the effect of long-term aging, which consists of a significant increase in the internal field, is caused by the ascending diffusion effect (the Gorsky effect) of positively charged oxygen vacancies.

Conflict of Interest

The authors declare that there is no conflict of interest, either existing or potential.

Author Contributions

The authors have made an equal contribution to the preparation of the paper.

Acknowledgments

Scanning electron microscopy was performed using the equipment of the Interdisciplinary Resource Center for Collective Use of Herzen State Pedagogical University of Russia (Modern Physical and Chemical Methods for the Research and Development of Materials for Industry, Science, and Education).

References

Akkopru-Akgun, B., Trolier-McKinstry, S. (2023) Tuning Nb solubility, electrical properties, and imprint through PbO stoichiometry in PZT films. *Materials*, 16 (11), article 3970. https://doi.org/10.3390/ma16113970 (In English)

Akkopru-Akgun, B., Zhu, W., Lanagan, M. T., Trolier-McKinstry, S. (2019) The effect of imprint on remanent piezoelectric properties and ferroelectric aging of $PbZr_{0.52}Ti_{0.48}O_3$ thin films. *Journal of the American Ceramic Society*, 102 (9), 5328–5341. https://doi.org/10.1111/jace.16367 (In English)

Alexe, M., Harnagea, C., Hesse, D., Gösele, U. (2001) Polarization imprint and size effects in mesoscopic ferroelectric structures. *Applied Physics Letters*, 79 (2), 242–244. https://doi.org/10.1063/1.1385184 (In English)

Araujo, E. B., Lima, E. C., Bdikin, I. K., Kholkin, A. L. (2016) Imprint effect in PZT thin films at compositions around the morphotropic phase boundary. *Ferroelectrics*, 498 (1), 18–26. https://doi.org/10.1080/00150193.2016.1166421 (In English)

Bursian, E. V., Zaikovskii, O. I., Makarov, K. V. (1969) Polarization of a ferroelectric plate by bending. *Izvestiya Rossijskoj akademii nauk. Seriya fizicheskaya*, 33 (7), 1098–1100. (In Russian)

Choi, C. H., Lee, J., Park, B. H., Noh, T. W. (1997) Asymmetric switching and imprint in (La,Sr)CoO_3/Pb(Zr,Ti)O_3/(La,Sr)CoO_3 heterostructures. *Integrated Ferroelectrics*, 18 (1-4), 39–48. https://doi.org/10.1080/10584589708221684 (In English)

Ehre, D., Lyahovitskaya, V., Tagantsev, A., Lubomirsky, I. (2007) Amorphous piezo- and pyroelectric phases of $BaZrO_3$ and $SrTiO_3$. *Advanced Materials*, 19 (11), 1515–1517. https://doi.org/10.1002/adma.200602149 (In English)

Frey, J., Schlenkrich, F., Schönecker, A. (2001) Self-polarization and texture of wet chemically derived lead zirconate titanate thin films. *Integrated Ferroelectrics*, 35 (1-4), 105–113. https://doi.org/10.1080/10584580108016892 (In English)

Gavrilyachenko, V. G., Dudkevich, V. P., Fesenko, E. G. (1968) Natural unipolarity of barium titanate single crystals grown by the Remeika method. *Kristallografiya*, 13 (2), 342–343. (In Russian)

Gorsky, W. S. (1935) Theorie des elastischen Nachwirkung in ungeordneten Mischkristallen (elastische Nachwirkung zweiter Art) [Theory of elastic after-effect in unordered mixed crystals (elastic after-effect of the second kind)]. *Physikalische Zeitschrift der Sowjetunion*, 8 (4), 457–471. (In German)

Gruverman, A., Rodriguez, B. J., Kingon, A. I. et al. (2003) Mechanical stress effect on imprint behavior of integrated ferroelectric capacitors. *Applied Physics Letters*, 83 (4), 728–730. https://doi.org/10.1063/1.1593830 (In English)

Hiboux, S., Muralt, P. (2001) Origin of voltage offset and built-in polarization in in-situ sputter deposited PZT thin films. *Integrated Ferroelectrics*, 36 (1-4), 83–92. https://doi.org/10.1080/10584580108015530 (In English)

Kanareikin, A. G., Kaptelov, E. Yu., Senkevich, S. V. et al. (2016) Influence of high-temperature annealing on the orientation of the unipolarity vector in lead zirconate titanate thin films. *Physics of the Solid State*, 58 (11), 2325–2330. http://doi.org/10.1134/S1063783416110147 (In English)

Kholkin, A. L., Brooks, K. G., Taylor, D. V. et al. (1998) Self-polarization effect in Pb(Zr,Ti)O_3 thin films. *Integrated Ferroelectrics*, 22 (1-4), 525–533. https://doi.org/10.1080/10584589808208071 (In English)

Kosevich, A. M. (1975) How a crystal flows. *Soviet Physics Uspekhi*, 17 (6), 920–930. (In English)

Lee, J., Ramesh, R. (1996) Imprint of (Pb,La)(Zr,Ti)O_3 thin films with various crystalline qualities. *Applied Physics Letters*, 68 (4), 484–486. https://doi.org/10.1063/1.116421 (In English)

Li, C.-L., Feng, G.-H. (2025) Hydrothermal engineering of ferroelectric PZT thin films tailoring electrical and ferroelectric properties via TiO_2 and $SrTiO_3$ interlayers for advanced MEMS. *Micromachines*, 16 (8), article 879. https://doi.org/10.3390/mi16080879 (In English)

Liu, L., Yi, J., Xu, K. et al. (2024) High piezoelectric property with exceptional stability in self-poled ferroelectric films. *Nature Communications*, 15, article 10798. https://doi.org/10.1038/s41467-024-54707-y (In English)

Okamura, S., Miyata, S., Mizutani, Y. et al. (1999) Conspicuous voltage shift of *D-E* hysteresis loop and asymmetric depolarization in Pb-based ferroelectric thin films. *Japanese Journal of Applied Physics*, 38 (9S), 5364–5367. https://doi.org/10.1143/JJAP.38.5364 (In English)

Pronin, I. P., Kaptelov, E. Yu., Tarakanov, E. A., Afanas'ev, V. P. (2002) Effect of annealing on the self-poled state in thin ferroelectric films. *Physics of the Solid State*, 44 (9), 1736–1740. https://doi.org/10.1134/1.1507258 (In English)

Scott, J. F. (1998) The physics of ferroelectric ceramic thin films for memory applications. *Ferroelectric Review*, 1 (1), 1–129. (In English)

Senkevich, S. V., Kiselev, D. A., Staritsyn, M. V. et al. (2024) Piezoelectric properties of spherulite thin films of lead zirconate titanate. *Physics of Complex Systems*, 5 (2), 60–66. https://doi.org/10.33910/2687-153X-2024-5-2-60-66 (In English)

Shen, G., Zhu, L., Wang, Z. et al. (2024) Tuning self-polarization of epitaxial $BiFeO_3$ thin films through interface effects. *ACS Applied Materials & Interfaces*, 16 (50), 70038–70046. https://doi.org/10.1021/acsami.4c14995 (In English)

Shvartsman, V. V., Pankrashkin, A. V., Afanasjev, V. P. et al. (2005) Piezoelectric properties of self-polarized Pb(Zr_xTi_{1-x})O_3 thin films probed by scanning force microscopy. *Integrated Ferroelectrics*, 69 (1), 103–111. https://doi.org/10.1080/10584580590897344 (In English)

Song, L., Glinsek, S., Defay, E. (2021) Toward low-temperature processing of lead zirconate titanate thin films: Advances, strategies, and applications. *Applied Physics Reviews*, 8 (4), article 041315. https://doi.org/10.1063/5.0054004 (In English)

Staritsyn, M. V., Fedoseev, M. L., Kiselev, D. A. et al. (2023a) Ferroelectric properties of lead zirconate titanate thin films obtained by RF magnetron sputtering near the morphotropic phase boundary. *Physics of the Solid State*, 65 (2), 290–295. https://doi.org/10.21883/PSS.2023.02.55414.531 (In English)

Staritsyn, M. V., Kiselev, D. A., Pronin, V. P. et al. (2023b) Features of the microstructure and properties of thin spherolite PZT films formed by a two-stage method of hf magnetron deposition. *Physical and Chemical Aspects of the Study of Clusters, Nanostructures and Nanomaterials*, 15, 196–206. https://doi.org/10.26456/pcascnn/2023.15.196 (In Russian)

Staritsyn, M. V., Pronin, V. P., Khinich, I. I. et al. (2023c) Microstructure of spherulitic lead zirconate titanate thin films. *Physics of the Solid State*, 65 (8), 1312–1318. https://doi.org/10.61011/PSS.2023.08.56577.140 (In English)

Stephanovich, V. A., Rodenbücher, C., Pilch, M. et al. (2023) Self-polarization in $PbTiO_3$ crystals induced by chemical inhomogeneity in the surface layer. *Crystals*, 13 (8), article 1155. https://doi.org/10.3390/cryst13081155 (In English)

Sun, S., Wang, Y., Fuierer, P. A., Tuttle, B. A. (1999) Annealing effects on the internal bias field in ferroelectric PZT thin films with self-polarization. *Integrated Ferroelectrics*, 23 (1-4), 25–43. https://doi.org/10.1080/10584589908210138 (In English)

Sviridov, E., Sem, I., Alyoshin, V. et al. (1994) Ferroelectric film self-polarization. *MRS Online Proceedings Library*, 361, 141–146. https://doi.org/10.1557/PROC-361-141 (In English)

Takayama, R., Tomita, Y., Iijima, K., Ueda, I. (1991) Pyroelectric properties and application to infrared sensors of $PbTiO_3$, $PbLaTiO_3$ and $PbZrTiO_3$ ferroelectric thin films. *Ferroelectrics*, 118 (1), 325–342. https://doi.org/10.1080/00150199108014770 (In English)

Tentilova, I. Yu., Kaptelov, E. Yu., Pronin, I. P., Ugolkov, V. L. (2012) Micropore formation in lead zirconate titanate films. *Inorganic Materials*, 48 (11), 1136–1140. https://doi.org/10.1134/S0020168512110155 (In English)

Valeeva, A. R., Kaptelov, E. Yu., Senkevich, S. V. et al. (2022) An influence of mechanical stresses on the magnitude of the internal field in lead zirconate titanate thin films. *Technical Physics Letters*, 48 (8), 37–39. https://doi.org/10.21883/TPL.2022.08.55058.19218 (In English)

Valeeva, A. R., Staritsyn, M. V., Senkevich, S. V. et al. (2025) Influence of bending deformation in spherulitic films of lead zirconate titanate on the formation of the internal field and self-polarization. *Materials of Physics and Mechanics*, 53 (6), 12–24. http://dx.doi.org/10.18149/MPM.5362025_2 (In English)

Warren, W. L., Dimos, D., Pike, G. E. et al. (1995) Voltage shifts and imprint in ferroelectric capacitors. *Applied Physics Letters*, 67 (6), 866–868. https://doi.org/10.1063/1.115531 (In English)

Yudin, P. V., Tagantsev, A. K. (2013) Fundamentals of flexoelectricity in solids. *Nanotechnology*, 24 (43), article 432001. https://doi.org/10.1088/0957-4484/24/43/432001 (In English)

Condensed Matter Physics.
Solid state physics

UDC 538.9

EDN JDXSII
https://www.doi.org/10.33910/2687-153X-2026-7-2-74-78

The influence of ultraviolet radiation on electrical relaxation processes within the temperature area of stained glass films of PET

I. A. Fedorov [1], N. P. Bebenin [1], A. V. Stepchenkova [1], E. A. Volgina [1], D. E. Temnov ✉[1]

[1] Herzen State Pedagogical University of Russia, 48 Moika Emb., Saint Petersburg 191186, Russia

Authors

Ivan A. Fedorov, e-mail: ivasispb@yandex.ru

Nikita P. Bebenin, e-mail: nikita2001bebenin@gmail.com

Anastasiya V. Stepchenkova, e-mail: nastyastep7@icloud.com

Elena A. Volgina, ORCID: 0000-0002-1536-5841, e-mail: volgina.elena.1999@mail.ru

Dmitry E. Temnov, ORCID: 0000-0002-9560-4346, e-mail: detem@yandex.ru

For citation: Fedorov, I. A., Bebenin, N. P., Stepchenkova, A. V., Volgina, E. A., Temnov, D. E. (2026) The influence of ultraviolet radiation on electrical relaxation processes within the temperature area of stained glass films of PET. *Physics of Complex Systems*, 7 (2), 74–78. https://www.doi.org/10.33910/2687-153X-2026-7-2-74-78 EDN JDXSII

Received 13 January 2026; reviewed 3 February 2026; accepted 3 February 2026.

Funding: The research was supported by an internal grant of Herzen State Pedagogical University of Russia (project No. 57-ВГ).

Abstract. The electrical relaxation processes observed in poly(ethylene terephthalate) were investigated using thermal activation spectroscopy. In the area of glass transition temperature of this polymer, two relaxation processes were detected — in the area of 60°C and 80°C. Ultraviolet radiation caused a significant change in the intensity of these processes. Relaxation around 60 °C is related to the glass transition process in the amorphous phase of poly(ethylene terephthalate). Relaxation in the region of 80 °C may be related to a part of the amorphous phase at the surface of crystals (rigid amorphous fraction) characterized by reduced mobility of molecular segments. After UV irradiation of this polymer, the relative content of this fraction increases substantially.

Keywords: poly(ethylene terephthalate), thermostimulated depolarization, glass transition temperature, UV radiation, electrical relaxation

Introduction

Poly(ethylene terephthalate) (PET) is one of the most widely used thermoplastic polymers due to its combination of mechanical, thermal and dielectric properties (Dhaka et al. 2022; Joseph et al. 2024). PET has applications in food and beverage packaging (Benyathiar et al. 2022), textile fibers (Sarioğlu, Kaynak 2017), optical and electronic films, as well as substrates for flexible electronics and energy-harvesting devices (Yakimets et al. 2010). Its stability in use, low cost and technological versatility are the reason for constant interest in studying the structure, relaxation mechanisms and durability of the material under the influence of external factors.

PET crystallization is accompanied by the formation of not only an ordered crystal phase and amorphous phase but also a limited amorphous phase with reduced segment mobility at the surface of the crystals, resulting in a three-component structure: crystalline, amorphous fraction and rigid amorphous fraction (RAF) (Heidrich, Gehde 2022). This morphology affects the segmental mobility of molecules in the amorphous phase, since molecular segments closer to the surface of the crystals have greater limitations compared to those in freer amorphous regions. This heterogeneity is clearly evident

in relaxation processes: in fully amorphous α-relaxation polymers, the glasswork-associated process can be regarded as relatively uniform; in semi-crystalline PET, relaxation dynamics are spatially heterogeneous and reflect the complex interaction between amorphous and crystalline phases through local motion distribution and relaxation times (Alves et al. 2002; Wei et al. 1994).

Such heterogeneity makes relaxation processes in PET particularly sensitive to external factors that can modify the local mobility of macromolecules and the chemical structure of chains. In particular, ultraviolet exposure leads to photo-oxidative degradation of PET, accompanied by chain rupture, forming carbonyl and hydroxyl groups (Rostampour et al. 2024). These processes mainly develop in the amorphous phase and near the interphase regions, which allows one to expect a significant influence of UV radiation on glazing and α-relaxation parameters in semi-crystalline PET.

Despite the large number of articles and researches dealing with the photodegradation of PET and the modification of its mechanical and optical properties by UV radiation, the influence of UV radiation on glass processes and segmental relaxation in semi-crystalline PET remains understudied. This determines the relevance of this work, aimed at studying the influence of UV-effects on relaxation processes in PET.

Methods and materials

Materials

The samples were made from Hostaphan RNK PTP 13-μm thickness film produced by Mitsubishi Polyester Films. Ultraviolet radiation was carried out in the air using LE30 lamps manufactured by Lisma (Saransk, Russia).

Methods

The TSC-II system of Setaram (France) was used to measure thermal depolarization currents (TDC). The process of measuring the depolarization currents of the samples under investigation involved several sequential procedures. In the electric field at E = 90 V/min over 2 min, the samples were polarized at a polarization temperature of T_p = 60 °C. Next, in the electric field, the film was cooled at a rate of 2 °C/min to a temperature of T_0 = −10 °C and then held for t = 1 min. The specimen was then heated at a rate of 9°C/min to a temperature of T_f = 110 °C. The current was recorded with a Keithley 6517E electrometer with a measurement accuracy of 10^{-14} A. All measurements were carried out in a vacuum chamber in the atmosphere of helium gas.

When there are complex overlapping processes, standard thermal current peak processing methods such as the Buchi method, heating rate variation method and initial rise method produce incorrect results. The optimization method described in the article was used to process data in this work (Volgina et al. 2026).

Results and discussion

Fig. 1 shows the TSC curves of unirradiated UV radiation from the PET film, polarized at 60 °C in an electric field of different voltages. The practically linear dependence of the current value on the electric field voltage indicates the dipole mechanism of relaxation processes occurring at this temperature interval.

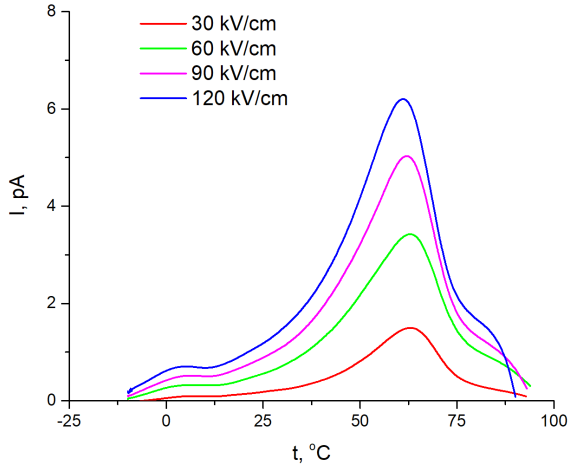

Fig. 1. The dependence of TSC for the original (unirradiated UV) PET film at different polarizing field values. Polarization temperature — 60 °C, heating rate — 9 °C/min

The data obtained clearly shows that the TSC curve is complex, indicating that several overlapping processes occur in the given temperature range as shown in Fig. 2(a). The following relaxations can be distinguished: in the areas of 10 °C (1), 40 °C (2), 60 °C (3) and 80 °C (4).

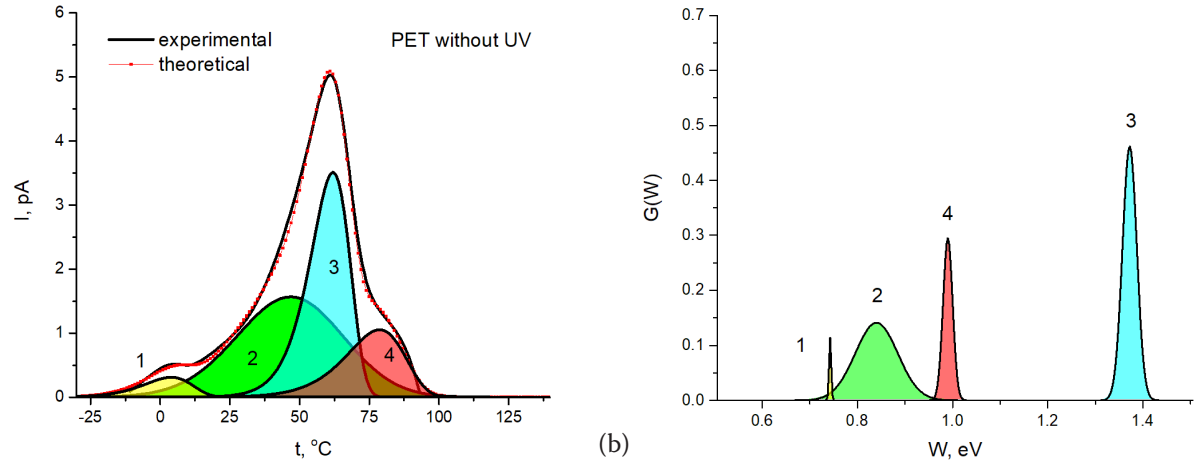

Fig. 2. a) Decomposition of the TSC curve for unirradiated PET polarized in the field 90 kV/cm at 60 °C to separate relaxation processes. b) The relaxer distribution functions for unirradiated UV polyethylene terephthalate processes as shown in Fig. 2(a)

At temperatures below the glass transition temperature T_g = 60 °C in a PET, only relaxation processes associated with the movement of macromolecular segments can occur (process 1). This is due to the fact that at temperatures below T_g the polymer is in a glass state, where the mobility of the chains is severely limited. As the temperature rises, different types of molecular motion begin to be activated: rotation of lateral groups, oscillatory movement of segments of the main chain and movement of entire macromolecule sections (process 2). At temperatures close to 60 °C, the TSC spectra show a peak corresponding to the process of glazing the amorphous part of the polymer (process 3). As previously mentioned, the presence of a crystalline part leads to the appearance of an amorphous part with limited segmental mobility and, as a consequence, to the emergence of a second relaxation process in the TSC currents associated with the glass transition process (process 4).

Fig. 2(b) presents the power distribution functions of G (W) relaxers involved in all the observed processes at temperatures ranging from -10 °C to 100 °C. The 'red' curve in Fig. 2(a) corresponds to the theoretical TSC curve calculated according to formula (1) and corresponding distribution functions in Fig. 2(b).

$$j(T) \sim \sum_{i}^{4} \int_{0}^{W_m} G_i(W) \exp\left[-\frac{W}{kT} - \int_{T_0}^{T} \frac{\omega_i}{\beta} \exp\left(-\frac{W}{kT'} \right) dT' \right] dW . \quad (1)$$

The high activation energy (W) for process 3 compared to process 4 is due to higher frequency factor values ($\omega_3 > \omega_4$).

Fig. 3 shows the TSC spectrum after the exposure of the samples to ultraviolet radiation from an unirradiated sample.

As is known, photo-oxidative degradation processes occur in PET due to the influence of UV radiation and are mainly accompanied by chain scission of macromolecules. This leads to increased mobility of the chain segments in the amorphous phase. The resulting shorter chains and fragments of macromolecules have an increased capacity for conformational relaxation. As a result, they can be regrouped and arranged in interlamellar regions, as well as near the crystal line, which is accompanied by a local increase in the degree of crystal personality.

According to the work (Falkenstein et al. 2020) performed using ATR-FTIR, NMR spectroscopy and enzymatic degradation analysis, UV treatment leads to the formation of a surface layer characterized by increased organization and relative increase in the proportion of the crystalline phase. This is related to photoinductive chain decompression and subsequent structural reorganization of the superficial regions.

 https://www.doi.org/10.33910/2687-153X-2026-7-2-74-78

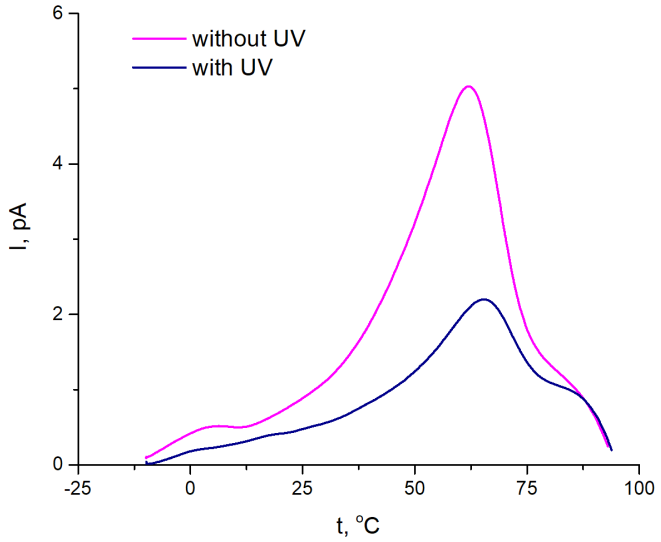

Fig. 3. TSC current dependence for the unirradiated and irradiated UV film of PET at 90 kV/cm polarizing field stress. Polarization temperature — 60 °C, heating rate — 9 °C/min

UV irradiation can lead to the redistribution of the phase composition of semi-crystalline PET: changing the ratio between a movable amorphous fraction, rigid amorphous fraction (RAF) and crystal phase, which potentially affects glazing parameters and α-relaxation characteristics.

Fig. 4(b) shows the power distribution functions of G (W) relaxants involved in all the observed processes at a temperature range from -10 °C to 100 °C. The 'red' curve in Fig. 4(a) corresponds to the theoretical TSC curve calculated according to formula (1) and corresponding distribution functions in Fig. 4b.

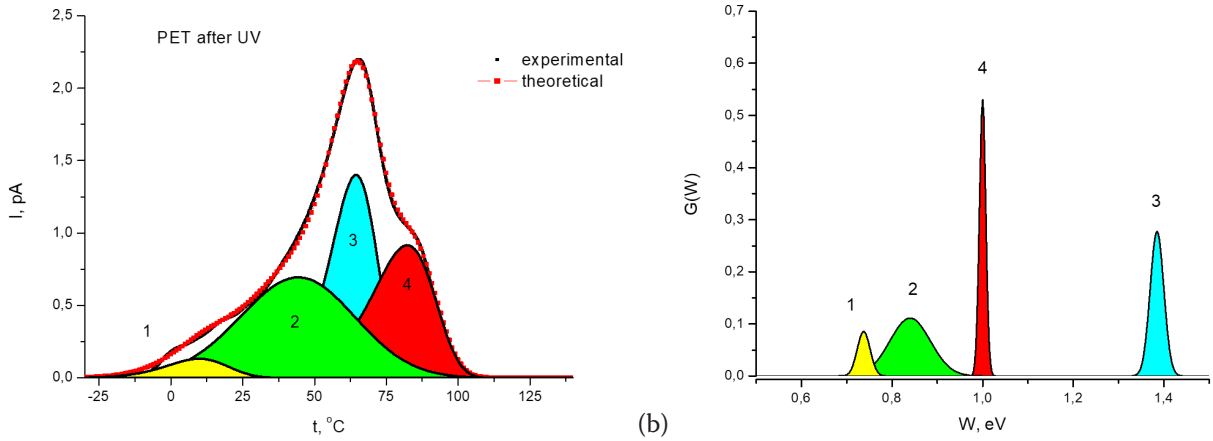

Fig. 4. a) Decomposition of the TDD curve for the irradiated UV PTEF polarized in the field E = 90 kV/cm at 60 °C for individual relaxation processes. b) The relaxer distribution functions for unirradiated UV polyethylene terephthalate processes as shown in Fig. 4(a)

For an unirradiated sample, the ratio between processes 4 and 3 is 4/3, whereas after UV irradiation, it decreases to 3/5. Therefore, the relative contribution of process 3 increases compared to process 4, indicating an increase in the RAF share in the irradiated sample.

Conclusion

Our research employed the method of thermally stimulated depolarization to study UV-irradiated and unirradiated PET films. The spectrum of TSC in the area 0 °C–100 °C demonstrates a complex character due to closely located overlapping relaxation processes. Relaxation processes in the area of 10 °C and 40 °C are observed below the glass transition temperature of this polymer and can only be related

to the movement of individual segments of macromolecules. Relaxation in the area of 60 °C and 80 °C is related to the processes of glass transition developing in the amorphous phase of the polymer and the so-called rigid amorphous fraction, which is on the border with available crystallites of the polymer. UV radiation of this polymer leads to a significant increase in the content of the limited amorphous phase, which indicates a local increase in the degree of crystallization of the polymer in the superficial regions. The functions of distribution of electrically active defects for all the relaxation processes were found by the optimization method.

Conflict of Interest

The authors declare that there is no conflict of interest, either existing or potential.

Author Contributions

All the authors discussed the final work and took part in writing the article.

References

Alves, N. M., Mano, J. F., Balaguer, E. et al. (2002) Glass transition and structural relaxation in semi-crystalline poly(ethylene terephthalate): A DSC study. *Polymer*, 43 (15), 4111–4122. (In English)

Benyathiar, P., Kumar, P., Carpenter, G. et al. (2022) Polyethylene terephthalate (PET) bottle-to-bottle recycling for the beverage industry: A review. *Polymers*, 14 (12), article 2366. https://doi.org/10.3390/polym14122366 (In English)

Dhaka, V., Singh, S., Anil, A. G. et al. (2022) Occurrence, toxicity and remediation of polyethylene terephthalate plastics: A review. *Environmental Chemistry Letters*, 20 (3), 1777–1800. https://doi.org/10.1007/s10311-021-01384-8 (In English)

Falkenstein, P., Gräsing, D., Bielytskyi, P. et al. (2020) UV pretreatment impairs the enzymatic degradation of polyethylene terephthalate. *Frontiers in Microbiology*, 11, article 689. https://doi.org/10.3389/fmicb.2020.00689 (In English)

Heidrich, D., Gehde, M. (2022) The 3-phase structure of polyesters (PBT, PET) after isothermal and non-isothermal crystallization. *Polymers*, 14 (4), article 793. https://doi.org/10.3390/polym14040793 (In English)

Joseph, T. M., Azat, S., Ahmadi, X. et al. (2024) Polyethylene terephthalate (PET) recycling: A review. *Case Studies in Chemical and Environmental Engineering*, 9, article 100673. https://doi.org/10.1016/j.cscee.2024.100673 (In English)

Rostampour, S., Cook, R., Jhang, S.-S. et al. (2024) Changes in the chemical composition of polyethylene terephthalate under UV radiation in various environmental conditions. *Polymers*, 16 (16), article 2249. https://doi.org/10.3390/polym16162249 (In English)

Sarioğlu, E., Kaynak, H. K. (2017) PET bottle recycling for sustainable textiles. In: N. O. Camlibel (ed.). *Polyester — production, characterization and innovative applications*. London: IntechOpen Publ., pp. 5–20. https://doi.org/10.5772/intechopen.72589 (In English)

Volgina, E. A., Temnov, D. E., Nechaev, A. N. et al. (2026) Effect of irradiation on cooperative relaxation in poly(vinylidene fluoride). *Radiation Physics and Chemistry*, 240, article 113413. https://doi.org/10.1016/j.radphyschem.2025.113413 (In English)

Wei, J., Delgado, R., Hawley, M. C. et al. (1994) Dielectric analysis of semi-crystalline poly(ethylene terephthalate). *MRS Online Proceedings Library*, 347 (1), 735–741. https://doi.org/10.1557/PROC-347-735 (In English)

Yakimets, I., MacKerron, D., Giesen, P. et al. (2010) Polymer substrates for flexible electronics: Achievements and challenges. *Advanced Materials Research*, 93-94, 5–8. https://doi.org/10.4028/www.scientific.net/AMR.93-94.5 (In English)

Physics of Semiconductors. Solid state physics

UDC 539.216+537.226.4

EDN SKNMEI
https://www.doi.org/10.33910/2687-153X-2026-7-2-79-83

Electrophysical properties of the Rochelle salt / zeolite A nanocomposite (Part 2)

T. G. Matveeva ✉[1], R. A. Castro Arata [2], V. G. Solovyev [3, 4]

[1] Pskov State University Branch in Velikiye Luki, 24 Novoslobodskaya Emb., Velikiye Luki 182100, Russia
[2] Herzen State Pedagogical University of Russia, 48 Moika Emb., Saint Petersburg 191186, Russia
[3] S. M. Budyonny Military Academy of Telecommunications, 3 Tikhoretsky Ave., Saint Petersburg 194064, Russia
[4] Pskov State University, 2 Lenina Sq., Pskov 180000, Russia

Authors

Tamara G. Matveeva, ORCID: 0009-0009-8382-1667, e-mail: mtg88@yandex.ru

Rene Alejandro Castro Arata, ORCID: 0000-0002-1902-5801, e-mail: recastro@mail.ru

Vladimir G. Solovyev, ORCID: 0000-0002-8452-6928, e-mail: solovyev_v55@mail.ru

For citation: Matveeva, T. G., Castro Arata, R. A., Solovyev, V. G. (2026) Electrophysical properties of the Rochelle salt / zeolite A nanocomposite (Part 2). *Physics of Complex Systems*, 7 (2), 79–83. https://www.doi.org/10.33910/2687-153X-2026-7-2-79-83 EDN SKNMEI

Received 13 January 2026; reviewed 3 February 2026; accepted 3 February 2026.

Funding: The article was prepared as part of the project 'Scientific and Educational Mathematical Center "Kovalevskaya North-West Center for Mathematical Research"' (agreement no. 075-02-2025-1607, 27 February 2025).

Abstract. This paper studies the electrical conductivity, permittivity, and dielectric losses of a nanocomposite obtained by impregnating a NaA zeolite host matrix with Rochelle salt (potassium sodium tartrate tetrahydrate, $KNaC_4H_4O_6 \times 4H_2O$) as a guest substance over the frequency range from 0.1 Hz to 1 MHz upon heating from 273 K to 493 K. This study discusses the characteristic features of the frequency and temperature dependences of the electrophysical properties of the Rochelle salt / zeolite A nanocomposite.

Keywords: ferroelectrics, Rochelle salt, permittivity, dielectric losses, electrical conductivity, zeolite, nanocomposite

Introduction

The matrix method for creating nanocomposite materials, proposed in the late 20th century (Bogomolov 1978; Stucky, Mac Dougall 1990), offers numerous advantages, including the ability to study ensembles of nanoparticles at high concentrations and with ultra-small sizes (up to 1 nm).

This paper employs this method to study size dependence of the upper ferroelectric Curie point T_C in the well-known crystalline substance — Rochelle salt (double potassium sodium tartrate $KNaC_4H_4O_6 \times 4H_2O$; RS in what follows) embedded into a NaA-type zeolite matrix.

Previous investigations have examined the ferroelectric properties of Rochelle salt dispersed in various porous media. In the case of RS embedded into a microporous glass matrix with particle diameters of ~ 7 nm ferroelectric features appeared only on the derivative ($d\varepsilon/dT$) curve (Colla et al. 1996). RS inclusions in nanoporous alumina with pore diameters from 10 to 40 nm retain a ferroelectric state at temperatures exceeding the Curie point of bulk crystals by several tens of degrees (Rogazinskaya et al. 2009). In contrast, a low-temperature shift of the Curie point T_C of the RS guest substance's upper ferroelectric transition due to confined geometry has been observed in mesoporous sieves MCM-41 with 2.6 nm pores (Tien et al. 2008), as well as in NaA zeolite (Matveeva, Solovyev 2022; Puchkov et al. 2025). NaA zeolite is a porous dielectric matrix containing an ordered system of interconnected voids and

three-dimensional channels with diameters of ~ 1 nm (Breck 1974). The lattice parameters of Rochelle salt ($a \approx 1.2$ nm, $b \approx 1.4$ nm, and $c \approx 0.6$ nm) (Solans et al. 1997) are rather large; thus, we assume that RS molecules can only reside within the α-cavities of the NaA crystal, where interactions between neighbouring molecules are possible.

In a previous work (Matveeva et al. 2024) we studied electrophysical properties of RS ferroelectric / zeolite NaA near the ferroelectric phase transition temperature over the frequency range from 100 Hz to 100 kHz. It was found that this nanocomposite shows a shift of the RS upper ferroelectric transition Curie point by ~ 5 K towards lower temperatures, relative to the phase transition temperature in a bulk ferroelectric (T_C = 297 K).

The present study aims to experimentally determine the electrophysical characteristics of this nanocomposite material over a wide range of frequencies (0.1 Hz–1 MHz) and temperatures (273–493 K).

Experiment

We used granules (~ 2 mm in diameter) of NaA zeolite as a porous dielectric host matrix. A saturated aqueous solution at room temperature introduced the Rochelle salt guest substance into the zeolite voids; thereafter, the ferroelectric / zeolite (RS / NaA) nanocomposite sample was washed with distilled water and dried at T = 300 K. To remove Rochelle salt from the sample surface, it was subjected to mechanical processing (surface grinding), and then shaped into a tablet with a diameter of 2 mm and a thickness of approximately 0.5 mm. After that, the sample was clamped between the metal electrodes of the measuring cell.

The complex dielectric permittivity was measured using a Novocontrol Concept 41 spectrometer at the Interdisciplinary Resource Center for Collective Use of Herzen State Pedagogical University of Russia (Modern Physical and Chemical Methods for the Research and Development of Materials for Industry, Science, and Education). The frequency range spanned from 0.1 Hz to 1 MHz, and measurements were conducted at controlled temperatures between 273 and 493 K.

Results and discussion

Figure 1 shows frequency dependences of the electrical conductivity for the RS ferroelectric / zeolite A nanocomposite in the ferroelectric and paraelectric phases. One can observe a power-law frequency dependence of conductivity, $\sigma \sim f^s$, which is often found in many materials (Jonscher 1972; Mott, Davis 1979) and may arise from two distinct mechanisms: (1) a rotational motion of molecular dipoles with frictional losses (when $s \approx 2$), and (2) a translational motion of free electric charges ($0 < s < 1$). For the experimental results shown in Fig. 1, $s \approx 1.3 (10^4\ Hz \le f \le 10^6\ Hz)$. This exponent value can be explained by the simultaneous existence of both mechanisms; a similar situation has already been observed in another ferroelectric material (Mostafa et al. 2005).

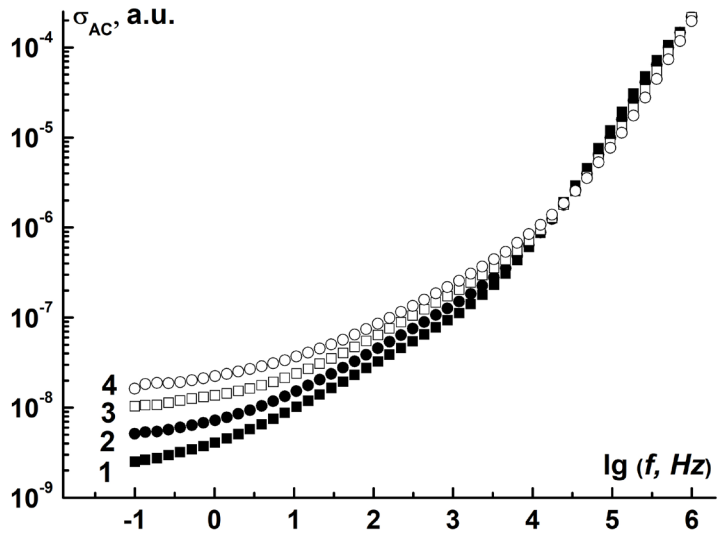

Fig. 1. Frequency dependences of the electrical conductivity for the RS / NaA composite at 283 K (curve 1), 293 K (curve 2), 303 K (curve 3), 313 K (curve 4)

 https://www.doi.org/10.33910/2687-153X-2026-7-2-79-83

The frequency dependences of the dielectric losses for the RS / NaA composite (Fig. 2) display a decrease at relatively low frequencies — up to approximately 10 kHz — after which tgδ begins to increase. A similar pattern is observed in the frequency dependences of the imaginary part of the permittivity (Fig. 3). This high-frequency increase can be explained by proton conductivity (Colomban, Novak 1988; Ovchinnikova et al. 1997). Figures 2 and 3 again show an increase in dielectric losses at low frequencies, as well as a shift of the graph minima toward higher frequencies at the phase transition of Rochelle salt to the paraelectric phase.

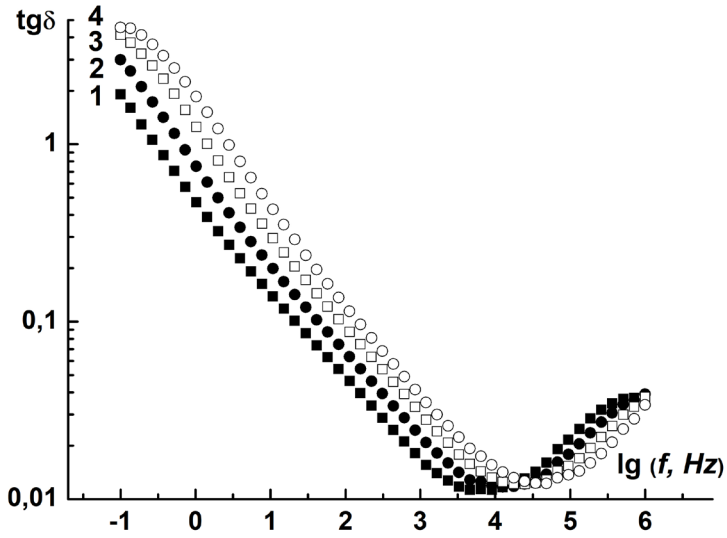

Fig. 2. Frequency dependences of the dielectric losses tgδ for the RS / NaA composite at 283 K (curve 1), 293 K (curve 2), 303 K (curve 3), 313 K (curve 4)

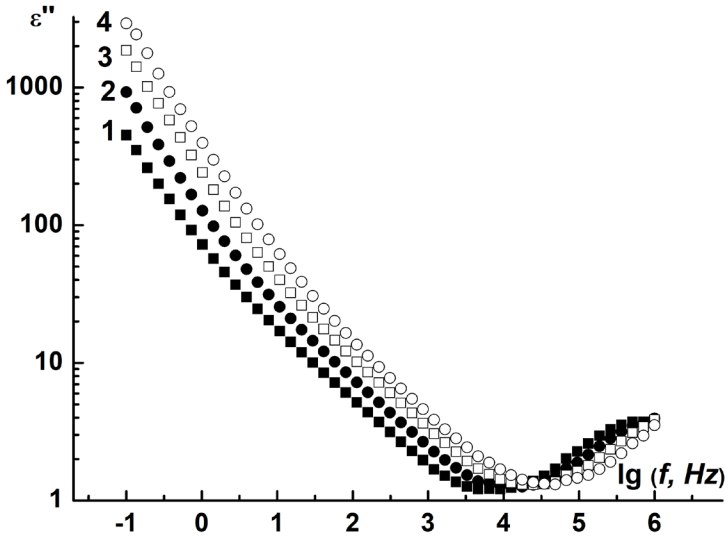

Fig. 3. Frequency dependences of the imaginary part of dielectric permittivity ε`` for the RS / NaA composite at 283 K (curve 1), 293 K (curve 2), 303 K (curve 3), 313 K (curve 4)

Figure 4 shows temperature dependences of the electrical conductivity for the RS / NaA composite at low frequencies. One can see two maxima at temperatures of approximately 323–333 and 363 K. It should be noted that at $T \approx 329$ K, Rochelle salt decomposes into a mixture of sodium and potassium tartrates (Jona, Shirane 1962); this process is often referred to as the 'melting' of Rochelle salt. According to our assumption, the second maximum likely corresponds to the subsequent stage of decomposition of these components. The temperature dependences of the dielectric losses (Fig. 5) exhibit similar peculiarities.

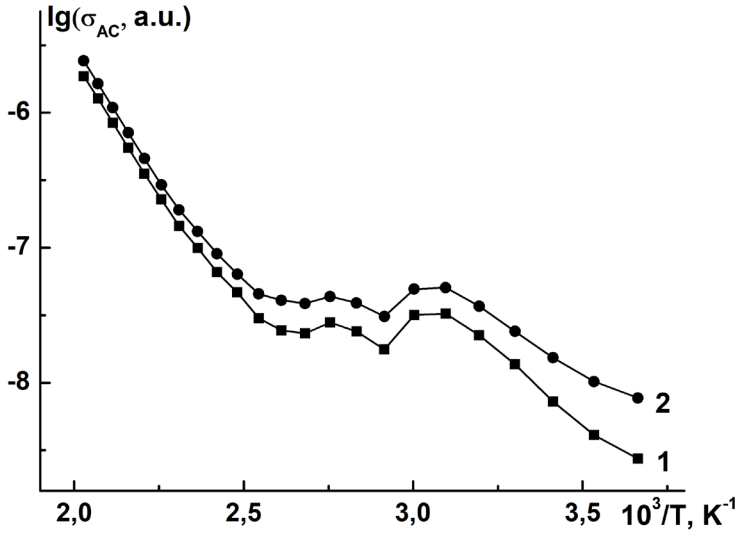

Fig. 4. Temperature dependences of the electrical conductivity for the RS / NaA composite at 1 Hz (curve 1) and 10.8 Hz (curve 2)

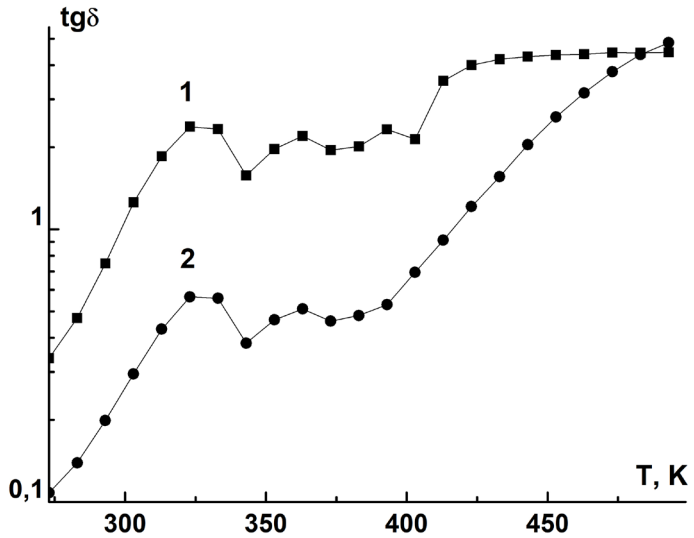

Fig. 5. Temperature dependences of the dielectric losses tgδ for the RS / NaA composite at 1 Hz (curve 1) and 10.8 Hz (curve 2)

Conclusions

The ferroelectric / zeolite nanocomposite material obtained by infiltrating the NaA zeolite host matrix with the Rochelle salt guest substance exhibits a power-law frequency dependence of electrical conductivity which can be explained by the simultaneous existence of two mechanisms: (1) rotational motion of dipoles with frictional losses, and (2) translational motion of free electric charges.

Upon heating from room temperature, the study observes a significant increase in dielectric losses at frequencies below 10 kHz, and this increase continues into the paraelectric phase.

Conflict of Interest

The authors declare that there is no conflict of interest, either existing or potential.

Author Contributions

All the authors discussed the final work and took part in writing the article.

 https://www.doi.org/10.33910/2687-153X-2026-7-2-79-83

References

Bogomolov, V. N. (1978) Liquids in ultrathin channels (Filament and cluster crystals). *Soviet Physics Uspekhi*, 21 (1), 77–83. https://doi.org/10.1070/PU1978v021n01ABEH005510 (In English)

Breck, D. W. (1974) *Zeolite molecular sieves: Structure, chemistry, and use*. New York: Wiley Publ., 771 p. (In English)

Colla, E. V., Koroleva, E. Yu., Kumzerov, Yu. A. et al. (1996) Ferroelectric phase transitions in materials embedded in porous media. *Ferroelectric, Letters Section*, 20 (5–6), 143–147. (In English)

Colomban, P., Novak, A. (1988) Proton transfer and superionic conductivity in solids and gels. *Journal of Molecular Structure*, 177, 277–308. https://doi.org/10.1016/0022-2860(88)80094-2 (In English)

Jona, F., Shirane, G. (1962) *Ferroelectric crystals*. Oxford; London; New York; Paris: Pergamon Press, 402 p. (In English)

Jonscher, A. K. (1972) Frequency-dependence of conductivity in hopping systems. *Journal of Non-Crystalline Solids*, 8–10, 293–315. (In English)

Matveeva, T. G., Ivanova, M. S., Solovyev, V. G., Vanin, A. I. (2024) Electrophysical properties of the Rochelle salt dispersed in a porous dielectric matrix of type A zeolite. *Physics of Complex Systems*, 5 (4), 195–201. https://doi.org/10.33910/2687-153X-2024-5-4-195-201 (In English)

Matveeva, T. G., Solovyev, V. G. (2022) Dielectric properties of the Rochelle salt nanoparticles in the NaA zeolite matrix. *Radio Communication Technology*, 4 (55), 118–124. https://doi.org/10.21667/2221-1241-2022-55-4-118-124 (In Russian)

Mostafa, M. F., Youssef, A. A. A., Montasser, S. S., Khyami, S. S. (2005) The frequency dependence of the conductivity and dielectric relaxation of $[(CH_2)_3(NH_3)_2]Cu(II)Cl_4$. *Zeitschrift für Naturforschung A*, 60 (11–12), 837–847. https://doi.org/10.1515/zna-2005-11-1213 (In English)

Mott, N. F., Davis, E. A. (1979) *Electron processes in non-crystalline materials*. 2nd ed. Oxford: Clarendon Press, 590 p. (In English)

Ovchinnikova, G. I., Gavrilova, N. D., Lotonov, A. N. et al. (1997) Ion transport as manifested in microwave spectra and static conduction of seignette salt crystals. *Bulletin of the Russian Academy of Sciences: Physics*, 61 (12), 1913–1917. (In English)

Puchkov, N. I., Matveeva, T. G., Vanin, A. I. et al. (2025) Size dependence of the Curie point of a system of Rochelle salt nanoparticles in porous dielectric matrices. *Glass Physics and Chemistry*, 51 (4), 486–490. https://doi.org/10.1134/S1087659625600541 (In English)

Rogazinskaya, O. V., Milovidova, S. D., Sidorkin, A. S. et al. (2009) Properties of nanoporous aluminum oxide with triglycine sulfate and Rochelle salt inclusions. *Physics of the Solid State*, 51 (7), 1518–1520. https://doi.org/10.1134/S1063783409070506 (In English)

Solans, X., Gonzalez-Silgo, C., Ruiz-Pérez, C. (1997) A structural study on the Rochelle salt. *Journal of Solid State Chemistry*, 131 (2), 350–357. (In English)

Stucky, G. D., Mac Dougall, J. E. (1990) Quantum confinement and host/guest chemistry: Probing a new dimension. *Science*, 247 (4943), 669–678. https://doi.org/10.1126/science.247.4943.669 (In English)

Tien, C., Charnaya, E. V., Lee, M. K. et al. (2008) NMR studies of structure and ferroelectricity for Rochelle salt nanoparticles embedded in mesoporous sieves. *Journal of Physics: Condensed Matter*, 20 (21), article 215205. https://doi.org/10.1088/0953-8984/20/21/215205 (In English)

Theoretical physics.
Physics of atoms and molecules

UDC 539.184

EDN ZTCZJC
https://www.doi.org/10.33910/2687-153X-2026-7-2-84-91

Nuclear magnetic shielding and quadratic Zeeman effect in helium-like ions

V. A. Agababaev ✉[1], D. A. Glazov [1, 2], M. M. Osiptsov [1], A. V. Volotka [1], V. M. Shabaev [3]

[1] ITMO University, 49 Kronverksky Ave., Saint Petersburg 197101, Russia
[2] Petersburg Nuclear Physics Institute named by B. P. Konstantinov of National Research Centre 'Kurchatov Institute', 1 mkr. Orlova roshcha, Gatchina 188300, Russia
[3] Saint Petersburg State University, 7–9 Universitetskaya Emb., Saint Petersburg 199034, Russia

Authors

Valentin A. Agababaev, ORCID: 0000-0003-3400-5910, e-mail: v.agababaev@yandex.ru

Dmitry A. Glazov, ORCID: 0000-0002-4158-6963, e-mail: glazov.d.a@gmail.com

Matvey M. Osiptsov, e-mail: osipcov.matvej@gmail.com

Andrey V. Volotka, ORCID: 0000-0001-8439-1472, e-mail: avolotka@gmail.com

Vladimir M. Shabaev, ORCID: 0000-0002-2769-6891, e-mail: v.shabaev@spbu.ru

For citation: Agababaev, V. A., Glazov, D. A., Osiptsov, M. M., Volotka, A. V., Shabaev, V. M. (2026) Nuclear magnetic shielding and quadratic Zeeman effect in helium-like ions. *Physics of Complex Systems*, 7 (2), 84–91. https://www.doi.org/10.33910/2687-153X-2026-7-2-84-91 EDN ZTCZJC

Received 13 January 2026; reviewed 3 February 2026; accepted 3 February 2026.

Funding: The work was supported by the Foundation for the Advancement of Theoretical Physics and Mathematics 'BASIS'.

Abstract. The quadratic Zeeman effect and hyperfine magnetic shielding are calculated in the ground $(1s)^2$ state of helium-like ions using perturbation theory. Numerical values are obtained for the nuclear charge range $Z = 6 - 32$. The Zeeman splitting is computed by solving the Dirac equation in the Coulomb field of an extended nucleus with B-splines from the DKB method. Leading-order contributions and one-photon-exchange corrections are treated within a rigorous QED approach. The calculated nuclear magnetic shielding constants can be used to determine nuclear magnetic moments, and the quadratic Zeeman effect is relevant for high-precision Penning-trap measurements of transition energies in He-like ions.

Keywords: Zeeman effect, *g* factor, highly charged ions, bound-state QED, nuclear magnetic shielding, hyperfine structure

Introduction

Bound-electron *g* factor, which mostly determines Zeeman splitting in highly charged ions, has been measured with increasing precision during the last two decades (Sturm et al. 2017). The relative experimental uncertainty has reached 2.4×10^{-11} in H-like carbon (Sturm et al. 2014), 0.7×10^{-10} in Li-like silicon (Glazov et al. 2019), and 0.24×10^{-9} in B-like tin (Morgner et al. 2025). The *g*-factor measurements already performed and anticipated in the near future, combined with the corresponding theoretical efforts, provide access to the fundamental constants and nuclear properties (Harman et al. 2018; Shabaev et al. 2015). In particular, nuclear magnetic moments can be determined with unprecedented precision from the *g* factors of few-electron ions (Quint et al. 2008; Werth et al. 2001). This task has become particularly relevant after a discrepancy was found between the recent measurement of the hyperfine splitting in H- and Li-like bismuth (Ullmann et al. 2017) and the most accurate theoretical prediction

(Volotka et al. 2012). This so-called 'hyperfine puzzle' has been resolved with the new value of ^{209}Bi nuclear magnetic moment (Skripnikov et al. 2018), which disagrees with the previously accepted one. The more general outcome of this work is that the uncertainty of the magnetic moment values determined by the nuclear magnetic resonance method can be significantly underestimated. Recently, a new value for ^{207}Pb has been determined (Fella et al. 2020) in strong disagreement with the tabulated value. The nuclear magnetic shielding for a bound electron in the 1*s* and some excited states was studied using a fully relativistic approach in Refs. (Moore 1999; Pyper 1999; Pyper, Zhang 1999). Later, detailed theoretical investigations have been presented for the ground state of H-like (Moskovkin, Shabaev 2006; Moskovkin et al. 2004; Yerokhin et al. 2011; 2012), He-like (Yerokhin et al. 2024), Li-like (Moskovkin et al. 2008a; 2008b), and B-like ions (Volchkova et al. 2017). In this work, we study the nuclear magnetic shielding for the ground state of He-like ions. The total magnetic moment is fully determined by the nucleus and the shielding constant in this case. Despite certain experimental difficulties, this allows one, in principle, to access directly the nuclear magnetic moment in high-precision Penning-trap measurements.

The nonlinear contributions to the Zeeman splitting can play an important role in high- precision measurements. In particular, the second- and third-order effects can be detected in the Penning-trap experiments with B-like ions (von Lindenfels et al. 2013). Recent measurement of the ground-state *g* factor in $^{40}Ar^{13+}$ (Arapoglou et al. 2019) was sensitive to the third-order contribution (Glazov et al. 2013; Varentsova et al. 2017; 2018). Subtraction of the second-order contribution (Agababaev et al. 2017; Glazov et al. 2013; Varentsova et al. 2018) was required to obtain the most precise up-to-date experimental value of the fine-structure transition energy in B-like argon (Egl et al. 2019; Micke et al. 2020).

The nonlinear Zeeman effects are enhanced by the closely spaced levels of the same parity — $^2P_{1/2}$ and $^2P_{3/2}$ in B-like ions — which are mixed by the external magnetic field. The same can happen with $n = 2$ levels in low- and middle-Z He-like ions. The quadratic Zeeman shift can thus be relevant for future high-precision measurements. Transition energies in He-like ions serve as a perfect probe of the many-electron QED effects and therefore attract much experimental and theoretical interest: see, e. g., Refs. (Beiersdorfer, Brown 2015; Epp et al. 2015; Kozhedub et al. 2019; Loetzsch et al. 2024; Machado et al. 2018; Malyshev et al. 2019; 2023; Yerokhin, Surzhykov 2019; Yerokhin et al. 2022) and references therein. In this work, we investigate the second-order Zeeman effect for the ground state of low- and middle-Z He-like ions. The excited states of He-like ions will be the subject of our future work.

Both the nuclear magnetic shielding and the quadratic contribution in a magnetic field represent the terms of the second order of perturbation theory. In addition to the one- electron part, we consider the first-order interelectronic-interaction correction. The results are obtained within the perturbation theory using the finite basis sets.

Relativistic units ($\hbar = 1$, $c = 1$, $m_e = 1$) and Heaviside charge unit [$\alpha = e^2/4\pi$, $e < 0$] are employed throughout the paper; $\mu_B = |e|/2m_e$ denotes the Bohr magneton, m_p is the proton mass, and m_e is written for clarity in the electron-to-proton mass ratio m_e/m_p.

Relativistic theory for He-like ions

We consider a helium-like ion in the ground $(1s)^2$ state. The relativistic perturbation theory offers the following expression for the ground-state energy, to first order in $1 / Z$:

$$E_{1s^2} = 2E_{1s}^{(0)} + \Delta E_{1ph}^{(1)} + \ldots, \tag{1}$$

where $E_{1s}^{(0)}$ is the single-electron energy in the 1*s* state. The one-photon-exchange correction is given by

$$\Delta E_{1ph}^{(1)} = \langle ab | I(0) | ab \rangle - \langle ba | I(\Delta_{ab}) | ab \rangle . \tag{2}$$

Here, *a* and *b* represent electron states — 1*s* with angular momentum projection ± 1/2, and $\Delta_{ab} = E_a - E_b$ is zero in the present case. The operator I is the interelectronic-interaction operator, which in the Feynman gauge takes the form

$$I(\omega, r_{12}) = \alpha (1 - \alpha_1 \cdot \alpha_2) \frac{exp(i|\omega| r_{12})}{r_{12}} . \tag{3}$$

Below, we focus on various aspects of the Zeeman effect in helium-like ions, such as the second-order shift in a magnetic field and nuclear magnetic shielding. These problems have been addressed before, including the second-order Zeeman effect in hydrogen-like ions (Feinberg et al. 1990; Grozdanov, Taylor 1986; Manakov, Zapryagaev 1976; Manakov et al. 1974; Szmytkowski 2002a; 2002b), the second- and third-order Zeeman effects in boron-like ions (Agababaev et al. 2017; Glazov et al. 2013; von Lindenfels et al. 2013; Varentsova et al. 2017; 2018), and the Zeeman splitting in hydrogen-, helium-, lithium-, and boron-like ions with nonzero nuclear spin (Moskovkin, Shabaev 2006; Moskovkin et al. 2004; 2008a; 2008b; Volchkova et al. 2017; Yerokhin et al. 2011; 2012; 2024). The present work brings into focus two-electron systems and computes the first-order electron-electron interaction, namely one-photon-exchange contribution.

For this purpose, we employ the complete spectrum of the one-electron Dirac equation

$$\widehat{H_0}\psi(r) = \varepsilon\psi(r) \tag{4}$$

with the zeroth-order Hamiltonian:

$$\widehat{H_0} = \boldsymbol{\alpha}\boldsymbol{p} + \beta + V_{nuc}(r)\,, \tag{5}$$

where α and β are the Dirac matrices, and $V_{nuc}(r)$ is the spherically symmetric electrostatic nuclear potential. The interaction between electrons is treated within the framework of perturbation theory (PT). To describe the ground state of a helium-like ion, we specifically take the sum of two one-electron zeroth-order energies and account for the electron-electron interaction in first-order PT.

Quadratic contribution to the Zeeman effect

Consider a bound electron in the presence of an external magnetic field. The system is described by the stationary Dirac equation (4), and the magnetic field is treated as a perturbation V_m:

$$V_m = \lambda U, \quad \lambda = \mu_B B, \quad U = \left[\boldsymbol{r}\times\boldsymbol{\alpha}\right]_z. \tag{6}$$

Within the perturbation theory, the energy $E(\lambda)$ can be expanded in a power series in λ,

$$\begin{aligned} E(\lambda) &= E^{(0)} + \Delta E^{(1)} + \Delta E^{(2)} + \ldots \\ &= E^{(0)} + \lambda g^{(1)} + \lambda^2 g^{(2)} + \ldots . \end{aligned} \tag{7}$$

The first-order contribution, which is conveniently expressed via the g factor,

$$E^{(1)} = \lambda g^{(1)}(M_J) = \mu_B B g M_J\,, \tag{8}$$

and the second-order term can also be written in terms of a dimensionless quantity — the g^2 coefficient,

$$E^{(2)} = \lambda^2 g^{(2)}(M_J) = (\mu_B B)^2 g^{(2)}(M_J)\,. \tag{9}$$

These calculations are carried out here for the 1s state using the previously developed numerical approach (Varentsova et al. 2018). We then turn to the ground state of He-like ions, evaluating the contribution from electron-electron interaction. In this case, the linear Zeeman effect vanishes, and the second-order coefficient is expressed as

$$g^{(2)}\left[(1s)^2\right] = g_0^{(2)}\left[(1s)^2\right] + \Delta g_{1ph}^{(2)}\left[(1s)^2\right], \tag{10}$$

where $g_0^{(2)}[(1s)^2] = 2g^{(2)}[1s]$ corresponds to the non-interacting electron case and follows from the second-order perturbation theory expression:

$$g^{(2)}(1s) = \Sigma_n' \frac{\langle a|U|n\rangle\langle n|U|a\rangle}{\varepsilon_a - \varepsilon_n}\,, \tag{11}$$

where $|a\rangle$ denotes the one-electron [1s] state, and the summation extends over the complete Dirac spectrum of states $|n\rangle$, excluding the reference state $|a\rangle = |1s\rangle$. The resulting coefficient $g^{(2)}$ is an even function of the angular momentum projection: $g^{(2)}(M_J) = g^{(2)}(-M_J)$.

 https://www.doi.org/10.33910/2687-153X-2026-7-2-84-91

The one-photon exchange correction to the $g^{(2)}$ coefficient is obtained from the set of diagrams displayed in Fig. 1. To evaluate this correction, we employ formal expressions derived within a rigorous QED framework. Up to symmetry coefficients, these expressions coincide with those in Ref. (Moskovkin et al. 2008a) after replacing the hyperfine interaction potential with the magnetic-field interaction potential appropriate for the quadratic Zeeman effect.

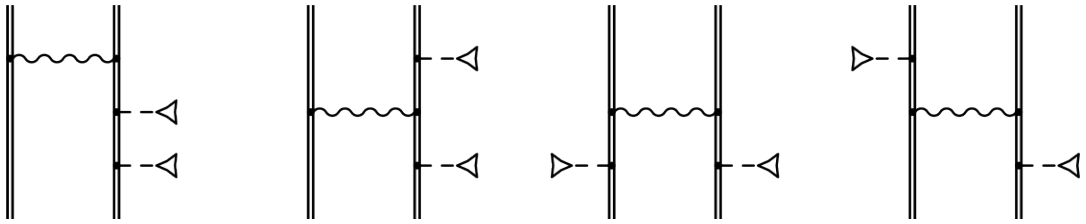

Fig. 1. Illustration of the one-photon exchange correction to the $g^{(2)}$ coefficient. In the diagram, the double line represents the electron propagator in the field of the nucleus $V_{nuc}(r)$, the wavy line corresponds to the photon propagator, and the dashed line terminating in a triangle denotes the interaction with the magnetic field as given in Eq. (6)

Zeeman splitting of the hyperfine structure levels

A rigorous treatment of the hyperfine interaction necessitates incorporating nuclear variables into the Hamiltonian. Nevertheless, after constructing the proper states of the system with a definite total angular momentum $\mathbf{F} = \mathbf{J} + \mathbf{I}$, the hyperfine interaction can be represented by an effective term within the Dirac Hamiltonian for the bound electron:

$$V_{hfs} = \mu W, \qquad \mu = \frac{\alpha}{2}\frac{m_e}{m_p} g_I I, \qquad W = \frac{[\boldsymbol{r}\times\boldsymbol{\alpha}]_z}{r^3}, \tag{12}$$

where I denotes the nuclear spin and g_I is the nuclear g factor. Note that μ represents a dimensionless parameter proportional (though not equal) to the nuclear magnetic moment.

Zeeman splitting of the hyperfine levels is then described by V_m in Eq. (6). The total perturbation potential in the Dirac equation is $V_m + V_{hfs}$. Within perturbation theory, the zeroth-order Hamiltonian remains that of Eq. (4), whereas the perturbation comprises two distinct contributions, V_m and V_{hfs}. These are governed by two independent parameters, λ and μ, which 'tune' the magnetic and hyperfine interactions, respectively.

In the present work, we consider the weak-magnetic-field regime, where the Zeeman splitting is significantly smaller than the hyperfine splitting. In this limit, the linear Zeeman shift is characterized by the g factor of the electron-nucleus system, which takes the form (Moskovkin et al. 2004; Yerokhin et al. 2012):

$$g_F = g_J \frac{F(F+1) - I(I+1) + J(J+1)}{2F(F+1)} - (1-\sigma)\frac{m_e}{m_p} g_I \frac{F(F+1) + I(I+1) - J(J+1)}{2F(F+1)}, \tag{13}$$

where g_J is the electronic g factor, while m_e and m_p denote the electron and proton masses, respectively. The nuclear magnetic shielding constant σ arises from the mixed second-order contribution involving the perturbations V_m and V_{hfs}. We compute σ for the 1s state using perturbation theory, following the previous work of our group (Volchkova et al. 2017). In the one-electron approximation, it is conveniently characterized by the relativistic factor $A(\alpha Z)$ (Shabaev 1994; Volotka et al. 2008), which can be expressed as:

$$A = \frac{3}{8(\alpha Z)^3 M_J}\langle a|W|a\rangle . \tag{14}$$

The expression for σ in the ground state of He-like ions is written as:

$$\sigma\left[(1s)^2\right] = \sigma_0\left[(1s)^2\right] + \Delta\sigma_{1ph}\left[(1s)^2\right], \tag{15}$$

where $\sigma_0[(1s)^2] = 2\sigma[1s]$ is obtained from the second-order perturbation theory term:

$$\sigma_0\left[1s\right] = \Sigma'_n \frac{\langle a|U|n\rangle\langle n|W|a\rangle}{\varepsilon_a - \varepsilon_n}, \tag{16}$$

where the summation extends over the complete spectrum of states $|n\rangle$, omitting the reference state $|a\rangle = |1s\rangle$, as in Eq. (11). Note that the first term in Eq. (13) vanishes because $J = 0$ in this case.

The diagrams illustrating the one-photon-exchange corrections to the nuclear magnetic shielding are shown in Fig. 2. Their explicit form can be found in Ref. (Moskovkin et al. 2008a).

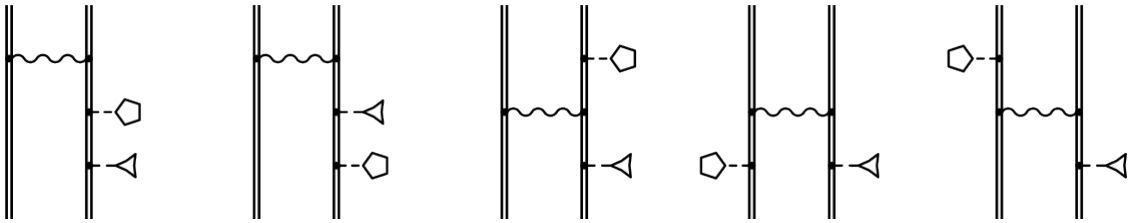

Fig. 2. Illustration of the one-photon-exchange correction to the nuclear magnetic shielding. Here, the hyperfine interaction potential (Eq. (12)) is represented by a dashed line terminating in a pentagon. The remaining notation is the same as in Fig. 1

Discussion

In this section, we present the results of our calculations for nuclear charge Z varying from 6 to 32. All the calculations were performed using B-splines obtained by the dual-kinetic-balance method (Shabaev et al. 2004). All calculations were performed for an extended nucleus, employing the homogeneously charged sphere model for the nuclear charge distribution.

Table 1 presents the values of the coefficient $g^{(2)}$, its one-photon-exchange correction, and their sum for the ground $(1s)^2$ state of helium-like ions. For convenience, g factor values for hydrogen-like ions are also listed. As expected from Eq. (11), $g^{(2)}$ scales as $(\alpha Z)^{-2}$ with increasing Z. It is important to note that the contribution of the negative-energy spectrum to this coefficient is dominant. The one-photon-exchange correction behaves as$1/Z$ as expected. Moreover, its relative magnitude is smaller than in the case of p states, where the coefficient is mainly determined by a single contribution whose energy denominator depends strongly on the interelectronic interaction.

Table 1. The g factor for the $1s$ state and the second-order Zeeman effect for the ground $(1s)^2$ state of helium-like ions are expressed in terms of $g^{(2)}$ coefficient, comprising the leading-order term $g_0^{(2)}$, the one-photon-exchange correction $\Delta g_{1ph}^{(2)}$, and their sum $g^{(2)}$

Z	$g[1s]$	$g_0^{(2)}[(1s)^2]$	$\Delta g_{1ph}^{(2)}[(1s)^2]$	$g^{(2)}[(1s)^2]$
6	1.998721	1040.605	138.744	1179.349
10	1.996445	372.913	30.038	402.951
12	1.994878	258.154	17.410	275.564
14	1.993024	188.959	10.984	199.943
16	1.990881	144.049	7.374	151.423
18	1.988448	113.259	5.191	118.450
20	1.985723	91.236	3.794	95.030
26	1.975782	52.906	1.767	54.673
32	1.963138	34.032	0.945	34.977

 https://www.doi.org/10.33910/2687-153X-2026-7-2-84-91

Table 2 presents data on the hyperfine magnetic shielding for the ground $(1s)^2$ state of helium-like ions, defined by the coefficient σ, as well as the one-photon-exchange correction to it and the sum of these contributions. The values of the coefficient $A(\alpha Z)$ for the hydrogen-like ion are given for comparison. As expected from (16), the coefficient σ scales linearly with Z. The one-photon-exchange correction behaves as $1/Z$ relative to σ, meaning that its absolute value does not vary significantly with Z.

Table 2. The factor $A(\alpha Z)$ for the 1s state and the nuclear magnetic shielding constant σ for the ground $(1s)^2$ state of helium-like ions. Presented here are the leading-order term $\sigma_0[(1s)^2]$, the one-photon-exchange correction $\Delta\sigma_{1ph}[(1s)^2]$, and their sum $\sigma[(1s)^2]$. The 1s results from Ref. (Moskovkin, Oreshkina, Shabaev et al. 2004) are shown for comparison ($\sigma_0[(1s)^2] = 2\sigma[1s]$). The values of σ are given in 10^{-3} units

Z	$A(\alpha Z)$	$\sigma_0[(1s)^2] \times 10^3$	$\Delta\sigma_{1ph}[(1s)^2] \times 10^3$	$\sigma[(1s)^2] \times 10^3$
6	1.002332	0.214108	–0.011041	0.203067
		0.214109[b]		
10	1.006906	0.360134	–0.010944	0.349190
	1.006911[a]	0.360135[b]		
12	1.010201	0.434893	–0.010875	0.424018
	1.010204[a]			
14	1.014136	0.511171	–0.010792	0.500379
	1.014133[a]			
16	1.018689	0.589235	–0.010693	0.578542

Note: [a]From Ref. (Volotka et al. 2008), [b]from Ref. (Moskovkin et al. 2004).

For comparison, we also present the values of the hyperfine-splitting factor A obtained in this work using perturbation theory, alongside those from Ref. (Volotka et al. 2008), as well as the values of $\sigma[1s]$ from Ref. (Moskovkin et al. 2004). One can see that these coefficients are in good agreement. The remaining discrepancies can be attributed to the fact that the coefficients in Refs. (Moskovkin et al. 2004; Volotka et al. 2008) were calculated for a pure Coulomb potential, whereas our values were computed for a finite nucleus.

It should be noted that our calculations account for the finite nuclear size (employing the finite-size nuclear potential V_{nucl}), but neglect the effect of the finite nuclear magnetic moment distribution (the Bohr–Weisskopf effect). Consequently, the quantity we report is actually $A(\alpha Z)(1 - \delta)$, where δ represents the nuclear size correction (Shabaev 1994; Volotka et al. 2008).

Conclusion

This work reports on the calculation of the quadratic Zeeman effect and hyperfine magnetic shielding in helium-like ions using perturbation theory. We have obtained numerical values for the ground $(1s)^2$ state in the nuclear charge range $Z = 6 – 32$. The DKB method to solve the Dirac equation in the Coulomb field with an extended nucleus has been applied to evaluate the Zeeman splitting in helium-like ions. We provide the leading-order contributions as well as the one-photon-exchange corrections, the latter being derived within a rigorous QED approach. The results for the nuclear magnetic shielding constant can be used to determine the nuclear magnetic moments. The quadratic Zeeman effect can be relevant for high-precision Penning-trap measurements of the transition energies in He-like ions. To provide complete theoretical background, corresponding calculations for excited states are needed, which is the subject of our future investigations.

Conflict of Interest

The authors declare that there is no conflict of interest, either existing or potential.

Author Contributions

All authors made an equivalent contribution to the preparation of the publication.

References

Agababaev, V. A., Volchkova, A. M., Varentsova, A. S. et al. (2017) Quadratic Zeeman effect in boronlike argon. *Nuclear Instruments and Methods in Physics Research Section B: Beam Interactions with Materials and Atoms,* 408, 70–73. https://doi.org/10.1016/j.nimb.2017.03.130 (In English)

Arapoglou, I., Egl, A., Höcker, M. et al. (2019) *g* factor of boronlike argon $^{40}Ar^{13+}$. *Physical Review Letters,* 122 (25), article 253001. https://doi.org/10.1103/PhysRevLett.122.253001 (In English)

Beiersdorfer, P., Brown, G. V. (2015) Experimental study of the x-ray transitions in the heliumlike isoelectronic sequence: Updated results. *Physical Review A*, 91 (3), article 032514. https://doi.org/10.1103/PhysRevA.91.032514 (In English)

Egl, A., Arapoglou, I., Höcker, M. et al. (2019) Application of the continuous Stern-Gerlach effect for laser spectroscopy of the $^{40}Ar^{13+}$ fine structure in a Penning trap. *Physical Review Letters,* 123 (12), article 123001. https://doi.org/10.1103/PhysRevLett.123.123001 (In English)

Epp, S. W., Steinbrügge, R., Bernitt, S. et al. (2015) Single-photon excitation of $K\,\alpha$ in heliumlike Kr^{34+}: Results supporting quantum electrodynamics predictions. *Physical Review A*, 92 (2), article 020502. https://doi.org/10.1103/PhysRevA.92.020502 (In English)

Feinberg, G., Rich, A., Sucher, J. (1990) Quadratic Zeeman effect in positronium. *Physical Review A,* 41 (7), 3478–3480. https://doi.org/10.1103/PhysRevA.41.3478 (In English)

Fella, V., Skripnikov, L. V., Nörtershäuser, W. et al. (2020) Magnetic moment of ^{207}Pb and the hyperfine splitting of $^{207}Pb^{81+}$. *Physical Review Research,* 2 (1), article 013368. https://doi.org/10.1103/PhysRevResearch.2.013368 (In English)

Glazov, D. A., Köhler-Langes, F., Volotka, A. V. et al. (2019) *g* factor of lithiumlike silicon: New challenge to bound-state QED. *Physical Review Letters*, 123 (17), article 173001. (In English)

Glazov, D. A., Volotka, A. V., Schepetnov, A. A. et al. (2013) *g* factor of boron-like ions: Ground and excited states. *Physica Scripta,* T156, article 014014. https://doi.org/10.1088/0031-8949/2013/T156/014014 (In English)

Grozdanov, T. P., Taylor, H. S. (1986) Second-order perturbation calculations for the hydrogenic Zeeman effect. *Journal of Physics B: Atomic and Molecular Physics*, 19 (24), 4075–4085. (In English)

Harman, Z., Sikora, B., Yerokhin, V. A. et al. (2018) The *g* factor of highly charged ions. *Journal of Physics: Conference Series,* 1138 (1), article 012002. (In English)

Kozhedub, Y. S., Malyshev, A. V., Glazov, D. A. et al. (2019) QED calculation of electron-electron correlation effects in heliumlike ions. *Physical Review A*, 100 (6), article 062506. https://doi.org/10.1103/PhysRevA.100.062506 (In English)

Loetzsch, R., Beyer, H. F., Duval, L. et al. (2024) Testing quantum electrodynamics in extreme fields using helium-like uranium. *Nature,* 625 (7996), 673–678. https://doi.org/10.1038/s41586-023-06910-y (In English)

Machado, J., Szabo, C. I., Santos, J. P. et al. (2018) High-precision measurements of $n = 2 \rightarrow n = 1$ transition energies and level widths in He- and Be-like argon ions. *Physical Review A*, 97 (3), article 032517. https://doi.org/10.1103/PhysRevA.97.032517 (In English)

Malyshev, A. V., Kozhedub, Y. S., Glazov, D. A. et al. (2019) QED calculations of the $n = 2$ to $n = 1$ x-ray transition energies in middle-Z heliumlike ions. *Physical Review A*, 99 (1), article 010501. https://doi.org/10.1103/PhysRevA.99.010501 (In English)

Malyshev, A. V., Kozhedub, Y. S., Shabaev, V. M. (2023) *Ab initio* calculations of the $2p_{3/2} \rightarrow 2s$ transition in He-, Li-, and Be-like uranium. *Physical Review A*, 107 (4), article 042806. https://doi.org/10.1103/PhysRevA.107.042806 (In English)

Manakov, N. L., Rapoport, L. P., Zapryagaev, S. A. (1974) Relativistic electromagnetic susceptibilities of hydrogen-like atoms. *Journal of Physics B: Atomic and Molecular Physics*, 7 (9), article 1076. https://doi.org/10.1088/0022-3700/7/9/019 (In English)

Manakov, N. L., Zapryagaev, S. A. (1976) A reduced Green function of the Dirac equation with a Coulomb potential. Second order Zeeman effect. *Physics Letters A*, 58 (1), 23–25. (In English)

Micke, P., Leopold, T., King, S. A. et al. (2020) Coherent laser spectroscopy of highly charged ions using quantum logic. *Nature*, 578 (7793), 60–65. https://doi.org/10.1038/s41586-020-1959-8 (In English)

Moore, E. A. (1999) Relativistic chemical shielding: Formally exact solutions for one-electron atoms of maximum total angular momentum for any principal quantum number. *Molecular Physics*, 97 (3), 375–380. https://doi.org/10.1080/00268979909482838 (In English)

Morgner, J., Tu, B., Moretti, M. et al. (2025) *g* factor of boronlike tin. *Physical Review Letters*, 134 (12), article 123201. https://doi.org/10.1103/PhysRevLett.134.123201 (In English)

Moskovkin, D. L., Oreshkina, N. S., Shabaev, V. M. et al. (2004) *g* factor of hydrogenlike ions with nonzero nuclear spin. *Physical Review A*, 70 (30), article 032105. https://doi.org/10.1103/PhysRevA.70.032105 (In English)

Moskovkin, D. L., Shabaev, V. M. (2006) Zeeman effect of the hyperfine-structure levels in hydrogenlike ions. *Physical Review A*, 73 (5), article 052506. https://doi.org/10.1103/PhysRevA.73.052506 (In English)

Moskovkin, D. L., Shabaev, V. M., Quint, W. (2008a) *g* factor of Li-like ions with a nonzero nuclear spin. *Optics and Spectroscopy*, 104 (5), 637–649. https://doi.org/10.1134/S0030400X08050019 (In English)

Moskovkin, D. L., Shabaev, V. M., Quint, W. (2008b) Zeeman effect of the hyperfine-structure levels in lithiumlike ions. *Physical Review A*, 77 (6), article 063421. https://doi.org/10.1103/PhysRevA.77.063421 (In English)

Pyper, N. C. (1999) Relativistic theory of nuclear shielding in one-electron atoms 1. Theoretical foundations and first-order terms. *Molecular Physics*, 97 (3), 381–390. https://doi.org/10.1080/00268979909482839 (In English)
Pyper, N. C., Zhang, Z. C. (1999) Relativistic theory of nuclear shielding in one-electron atoms 2. Analytical and numerical results. *Molecular Physics*, 97 (3), 391–413. https://doi.org/10.1080/00268979909482840 (In English)
Quint, W., Moskovkhin, D. L., Shabaev, V. M., Vogel, M. (2008) Laser-microwave double-resonance technique for *g*-factor measurements in highly charged ions. *Physical Review A*, 78 (3), article 032517. https://doi.org/10.1103/PhysRevA.78.032517 (In English)
Shabaev, V. M. (1994) Hyperfine structure of hydrogen-like ions. *Journal of Physics B: Atomic, Molecular and Optical Physics*, 27 (24), 5825–5832. https://doi.org/10.1088/0953-4075/27/24/006 (In English)
Shabaev, V. M., Glazov, D. A., Plunien, G., Volotka, A. V. (2015) Theory of bound-electron *g* factor in highly charged ions. *Journal of Physical and Chemical Reference Data,* 44 (3), article 031205. https://doi.org/10.1063/1.4921299 (In English)
Shabaev, V. M., Tupitsyn, I. I., Yerokhin, V. A. et al. (2004) Dual kinetic balance approach to basis-set expansions for the Dirac equation. *Physical Review Letters,* 93 (13), article 130405. https://doi.org/10.1103/PhysRevLett.93.130405 (In English)
Skripnikov, L. V., Schmidt, S., Ullmann, J. et al. (2018) New nuclear magnetic moment of ^{209}Bi: Resolving the bismuth hyperfine puzzle. *Physical Review Letters,* 120 (9), article 093001. https://doi.org/10.1103/PhysRevLett.120.093001 (In English)
Sturm, S., Köhler, F., Zatorski, J. et al. (2014) High-precision measurement of the atomic mass of the electron. *Nature*, 506 (7489), 467–470. https://doi.org/10.1038/nature13026 (In English)
Sturm, S., Vogel, M., Köhler-Langes, F. et al. (2017) High-precision measurements of the bound electron's magnetic moment. *Atoms*, 5 (1), article 4. (In English)
Szmytkowski, R. (2002a) Magnetizability of the relativistic hydrogen-like atom: Application of the Sturmian expansion of the first-order Dirac-Coulomb Green function. *Journal of Physics B: Atomic, Molecular and Optical Physics*, 35 (5), 1379–1391. https://doi.org/10.1088/0953-4075/35/5/319 (In English)
Szmytkowski, R. (2002b) Larmor diamagnetism and Van Vleck paramagnetism in relativistic quantum theory: The Gordon decomposition approach. *Physical Review A*, 65 (3), article 032112. https://doi.org/10.1103/PhysRevA.65.032112 (In English)
Ullmann, J., Andelkovic, Z., Brandau, C. et al. (2017) High precision hyperfine measurements in bismuth challenge bound-state strong-field QED. *Nature Communications*, 8 (1), article 15484. (In English)
Varentsova, A. S., Agababaev, V. A., Glazov, D. A. et al. (2018) Interelectronic-interaction contribution to the nonlinear Zeeman effect in boronlike ions. *Physical Review A*, 97 (4), article 043402. (In English)
Varentsova, A. S., Agababaev, V. A., Volchkova, A. M. et al. (2017) Third-order Zeeman effect in highly charged ions. *Nuclear Instruments and Methods in Physics Research Section B: Beam Interactions with Materials and Atoms,* 408, 80–83. https://doi.org/10.1016/j.nimb.2017.05.040 (In English)
Volchkova, A. M., Varentsova, A. S., Zubova, N. A. et al. (2017) Nuclear magnetic shielding in boronlike ions. *Nuclear Instruments and Methods in Physics Research Section B: Beam Interactions with Materials and Atoms,* 408, 89–92. https://doi.org/10.1016/j.nimb.2017.04.086 (In English)
Volotka, A. V., Glazov, D. A., Andreev, O. V. et al. (2012) Test of many-electron QED effects in the hyperfine splitting of heavy high-*Z* ions. *Physical Review Letters,* 108 (7), article 073001. https://doi.org/10.1103/PhysRevLett.108.073001 (In English)
Volotka, A. V., Glazov, D. A., Tupitsyn, I. I. et al. (2008) Ground-state hyperfine structure of H-, Li-, and B-like ions in the intermediate-*Z* region. *Physical Review A*, 78 (6), article 062507. https://doi.org/10.1103/PhysRevA.78.062507 (In English)
Von Lindenfels, D., Wiesel, M., Glazov, D. A. et al. (2013) Experimental access to higher-order Zeeman effects by precision spectroscopy of highly charged ions in a Penning trap. *Physical Review A*, 87 (2), article 023412. https://doi.org/10.1103/PhysRevA.87.023412 (In English)
Werth, G., Häffner, H., Hermanspahn, N. et al. (2001) The *g* factor of hydrogenic ions: A test of bound state QED. In S. G. Karshenboim, F. Bassani, F. Pavone et al. (eds.). *The hydrogen atom: Precision physics of simple atomic systems*. Berlin; Heidelberg: Springer Publ., pp. 204–220. https://doi.org/10.1007/3-540-45395-4_11 (In English)
Yerokhin, V. A., Pachucki, K., Harman, Z., Keitel, C. H. (2011) QED theory of the nuclear magnetic shielding in hydrogenlike ions. *Physical Review Letters,* 107 (4), article 043004. https://doi.org/10.1103/PhysRevLett.107.043004 (In English)
Yerokhin, V. A., Pachucki, K., Harman, Z., Keitel, C. H. (2012) QED calculation of the nuclear magnetic shielding for hydrogenlike ions. *Physical Review A*, 85 (2), article 022512. https://doi.org/10.1103/PhysRevA.85.022512 (In English)
Yerokhin, V. A., Pachucki, K., Harman, Z., Keitel, C. H. (2024) Nuclear magnetic shielding in heliumlike ions. *Physical Review A*, 109 (3), article 032808. https://doi.org/10.1103/PhysRevA.109.032808 (In English)
Yerokhin, V. A., Patkóš, V., Pachucki, K. (2022) QED calculations of energy levels of heliumlike ions with $5 \le z \le 30$. *Physical Review A*, 106 (2), article 022815. https://doi.org/10.1103/PhysRevA.106.022815 (In English)
Yerokhin, V. A., Surzhykov, A. (2019) Theoretical energy levels of 1*sns* and 1*snp* states of helium-like ions. *Journal of Physical and Chemical Reference Data*, 48 (3), article 033104. https://doi.org/10.1063/1.5121413 (In English)

Problems of Physics Education.
Pedagogy of a comprehensive school

UDC 372.853+378

EDN XLKEIV
https://www.doi.org/10.33910/2687-153X-2026-7-2-92-100

Between astronomy and astrology: Preservice teachers' misconceptions about celestial objects

A. N. Krushelnitckii ✉[1], T. D. Razboinikova [1], A. I. Kolesnikova [2]

[1] Herzen State Pedagogical University of Russia, 48 Moika Emb., Saint Petersburg 191186, Russia
[2] State budgetary educational institution Lyceum No. 533 'Malaya Okhta Educational Complex', 31 Novocherkassky Ave., Saint Petersburg 195112, Russia

Authors

Artemii N. Krushelnitckii, ORCID: 0000-0003-3543-8531, e-mail: ak.spb.ru@gmail.com

Tatiana D. Razboinikova, ORCID: 0009-0006-6987-5659, e-mail: taniraizbainn@gmail.com

Anna I. Kolesnikova, ORCID: 0009-0002-4410-375X, e-mail: an.lavrova2018@yandex.ru

For citation: Krushelnitckii, A. N., Razboinikova, T. D., Kolesnikova, A. I. (2026) Between astronomy and astrology: Preservice teachers' misconceptions about celestial objects. *Physics of Complex Systems*, 7 (2), 92–100. https://www.doi.org/10.33910/2687-153X-2026-7-2-92-100 EDN XLKEIV

Received 13 January 2026; reviewed 3 February 2026; accepted 3 February 2026.

Funding: The study did not receive any external funding.

Abstract. This article addresses the persistence of astronomical misconceptions among preservice teachers. The study makes two contributions: 1) an object-based classification framework is proposed (Stars & Constellations, Moon, Solar System, Sun), grounded in cognitive theory and aligned with standard curricula; 2) the prevalence of misconceptions is illustrated through survey data from 69 students at Herzen State Pedagogical University of Russia. The survey instrument is not psychometrically validated and serves to document a precedent rather than measure population-level prevalence. Results show that 68.1% of respondents conflate zodiac signs with astronomical constellations, and 42% agree with the notion of astrology as a 'gateway' to astronomy. Cognitive mechanisms underlying the myth persistence (naive theories, synthetic models, p-prims) are discussed, along with five pedagogical strategies for addressing misconceptions in teacher training.

Keywords: astronomical misconceptions, astrology, teacher training, pedagogical strategies, scientific literacy, misconception classification, cognitive mechanisms

Introduction

Astronomy has long been recognized as one of the most captivating subfields of physics, sparking immense fascination among learners across all age groups (Hennig et al. 2023). Due to this high level of interest, recent educational reforms in various countries, including Russia, have sought to strengthen the role of astronomy within the core school curriculum. However, a persistent problem remains: despite formal pedagogical efforts, astronomical misconceptions — alternative conceptions, children's ideas, naive beliefs, etc. — are unusually resistant to change (Sadler et al. 2009). These misconceptions are not merely isolated errors but deep-seated beliefs that contradict accepted scientific information (Comins 1998; Driver 1989).

This challenge extends beyond physics classrooms. In an era where pseudoscientific beliefs — such as astrology — are resurging in popularity, misconceptions about celestial phenomena are increasingly pervasive among educators of all disciplines.

Astrology, defined as a 'doctrine concerning the influence of the mutual positions of the planets, the Moon, and the Sun, as well as their locations against the background of bright stars in various constellations, on natural phenomena (such as rainfall, droughts, earthquakes, etc.) and on the destinies

of individual people and entire nations' (Zhukov 2021, 60), is often conflated with astronomy in public discourse. While astronomy is a rigorous scientific discipline grounded in empirical evidence, astrology is widely regarded as a pseudoscience by the scientific community.

This conflation poses a significant challenge for secular education systems, which aim to foster scientific literacy and critical thinking while respecting diverse cultural beliefs.

The challenge is further complicated by the fact that not only preservice physics teachers but educators across disciplines — those responsible for guiding student conceptual development — often harbor the same misconceptions as their pupils (Hennig et al. 2023; Nandi et al. 2015; Parker, Heywood 1998). Research indicates a significant gap between a teacher's ability to perform formal tasks, such as ranking astronomical objects by size, and their ability to provide accurate qualitative explanations for celestial phenomena (Rajpaul et al. 2014). Moreover, teachers tend to dramatically overestimate student performance, largely because they remain unaware of the specific, entrenched misconceptions their students hold (Sadler et al. 2009). A classic illustration of this phenomenon is the documentary *A Private Universe*.

In this context, our study addresses the urgent need to equip educators with tools to distinguish scientific knowledge from pseudoscientific claims. We focus on the classification of astronomical misconceptions, with particular attention to the cultural and cognitive factors that perpetuate these myths.

This study makes two contributions: 1) it proposes an object-based classification framework for astronomical misconceptions, grounded in cognitive theory and aligned with standard curricula; 2) it illustrates the persistence of these misconceptions through survey data from 69 students (preservice teachers) at Herzen University. By proposing pedagogical strategies, we aim to support teachers in fostering a scientific worldview — one that embraces empirical inquiry while leaving questions of religious or metaphysical belief to personal conviction.

Illustrative pilot survey

This pilot survey serves as an illustrative case rather than a representative study. Its purpose is to demonstrate that astronomical misconceptions — particularly the conflation of astronomy and astrology — persist among preservice teachers across disciplines.

Survey design

To explore the prevalence of astronomical misconceptions among future educators, we conducted an anonymous online survey of 69 students (aged 17–28) from one pedagogical university, representing 17 academic programs across bachelor's and master's levels (Table).

Table. Distribution of survey participants by year and level of study (count of participants)

Field of study	Bachelor's level				Master's level	
	1st year	2nd year	3rd year	4th year	1st year	2nd year
Preschool and primary education	1	—	—	—	—	—
Special education	2	—	1	—	—	—
Foreign language teaching	—	1	3	—	—	—
Information technology and labor education	1	—	1	1	—	—
History and social sciences teaching	—	5	1	1	—	—
Theater and music arts education	1	—	—	—	—	—
Psychology	3	2	—	—	—	—
Physics	3	3	11	4	—	1
Physical education (Sports)	1	—	—	—	—	—
Philosophy education	—	—	—	—	—	1
Fine Art education	—	3	—	—	—	—
Economics and educational management	—	—	—	—	1	—
Life safety education	1	—	—	—	—	—
Mathematics teaching	5	1	—	—	—	—
Geography teaching	—	—	—	1	—	—
Philology	2	1	2	1	—	—
Law (Legal studies)	—	1	1	1	—	—

The survey was distributed through closed university chat groups to limit access to enrolled students only and prevent third-party responses. Participation was voluntary, and no incentives were offered. A preamble to the survey informed participants about the study's purpose, the anonymous nature of data collection, and their right to discontinue at any time. Completion of the survey was taken as implicit consent. No personally identifiable information was collected, and all data were aggregated for analysis.

The study was conducted with the approval of the department leadership. Given the minimal-risk nature of the survey (anonymous, non-sensitive educational topics) and the absence of vulnerable populations, formal institutional review board approval was not required under local guidelines at the time of data collection. However, we acknowledge this as a limitation.

The survey comprised 18 questions, including 3 demographic items (program, year, age) and 10 questions on astrological beliefs and astronomy knowledge.

In addition, students were asked an open-ended question: 'Are there people in your social circle who believe in astrology, numerology, or Tarot cards? (If yes, specify what they believe in and describe any instances from life when predictions came true.)'

At the end of the survey, students were given the opportunity to provide an open-ended response to the question: 'If you do not believe in astrology, where does your knowledge of it come from?'

The responses cited below include answers to these questions.

The full survey instrument (in Russian with English translations for international readers) has been deposited in the Zenodo repository (Krushelnitckii, Razboinikova 2026).

Key findings

Zodiac literacy and cultural ubiquity

All respondents identified their zodiac sign, reflecting the pervasive cultural penetration of astrological terminology. When asked whether they inquire about peers' zodiac signs, 75.4% in our sample answered affirmatively, with comments like:

— *'My parents are very compatible, so my mom thinks their zodiac signs played a part in making their marriage work.'* (B.Ed. 2nd-year student, History and social sciences teaching)

— *'It's more about general knowledge and being able to hold a conversation on almost any topic with just about anyone.'* (B.Ed. 4th-year student, Geography teaching)

This aligns with prior research on astrology's role as a social lubricant, but our data highlights its normalization among future teachers.

Blurred boundaries: Astronomy vs. astrology

A key misconception was revealed by the task: 'Match birth date periods with zodiac signs' and the follow-up question: 'When does the Sun pass through the constellation Aries?'

The task included a decoy date range resembling Cancer's zodiac period but actually corresponding to the Sun's passage through Gemini. This tested whether students distinguish astronomical constellations from astrological signs.

In our sample, 68.1% of respondents conflated the two, demonstrating persistent confusion:

— *'[I have] no knowledge of astrology at all. But I'm interested in the concept of tarot — it'd be cool to understand how the cards are chosen to determine a person's possible fate during a reading. But I don't take fortune-telling seriously. Oh, and I just happened to learn the zodiac signs. That's not astrology, right?'* (B.Ed. 2nd-year student, Philology)

This echoes Vosniadou's (Vosniadou 1994) 'synthetic models', where students merge scientific terms with pseudoscientific narratives.

Personal encounters with occult practices

Open-ended responses also revealed divergent attitudes toward astrology's legitimacy:

— *Endorsement*. A physics student (B.Ed. 2nd-year student) described their *'full natal chart reading'* as *'100% accurate to my personality'*, linking it to their astrological trust.

— *Skepticism*. A bachelor 1st-year student (Life Safety education) noted: *'I believe that astrology cannot be reliable, as we can take the date and time of birth as a starting point. Doctors record this time by rounding it off, whereas astrology requires precise timing for its calculations. Consequently, any conclusions drawn by astrology may fundamentally be incorrect.'* At the same time, she has friends in her social circle who are interested in tarot cards and astrology.

 https://www.doi.org/10.33910/2687-153X-2026-7-2-92-100

The Kepler paradox

When presented with Kepler's quote on astronomy's reliance on astrology for public appeal, 42% in our sample agreed, framing astrology as a 'gateway' to science:

- *'Astrology can be considered a science equal to astronomy.'* (B.Ed. 1st-year student, Physics)
- *'Astrology sparks people's interest in astronomy.'* (B.Ed. 3rd-year student, Foreign language teaching)
- *'...at present, astronomy as a science is capable of standing on its own due to people's awareness of the importance of space exploration. However, I agree with the idea that the serious branches of any science rely on an engaging presentation of its fundamentals, be it popular science or astrology.'* (B.Ed. 3rd-year student, Physics)
- *'I believe that astrology is scientifically flawed, but at the same time it helps the development of astronomy.'* (B.Ed. 3rd-year student, Physics)

These responses illustrate a paradoxical relationship between astrology and astronomy in the eyes of preservice teachers. Some participants — including physics students — view astrology as a catalyst for public interest in science, echoing Kepler's historical observation about its role in sustaining astronomy's appeal. Their comments reveal a pragmatic stance: astrology, despite its scientific flaws, is perceived as a cultural bridge that can engage audiences who might otherwise disregard astronomy.

While our small-scale data precludes generalization, it establishes a precedent: future teachers, regardless of the discipline, may actively endorse pseudoscientific beliefs. This finding aligns with prior Russian research documenting similar patterns of astronomical misconceptions among preservice teachers at pedagogical universities (Nandi et al. 2015).

These misconceptions are particularly concerning among preservice teachers, whose future students may inherit these blurred boundaries. As prior research indicates (Comins 2001; Vosniadou 1994), such synthetic models — where scientific and nonscientific ideas coexist — can hinder the development of a coherent scientific worldview.

Limitations

Several methodological limitations should be acknowledged.

First, the sample size (69 participants) and single-institution design limit statistical power and generalizability. The voluntary nature of participation may have introduced self-selection bias, as students with stronger opinions on astrology — either positive or negative — may have been more likely to complete the survey.

Second, the open-ended responses were analyzed thematically without formal intercoder reliability procedures, as the number of substantive responses was limited. Third, all data are self-reported, which may be subject to social desirability bias, particularly on questions about belief in pseudoscience. Finally, the cross-sectional design precludes causal inferences about how misconceptions develop or change over the course of teacher training.

Third, the survey questions were designed to illustrate the persistence of astronomical misconceptions rather than measure their prevalence. The instrument was not validated psychometrically; its purpose was to document concrete examples of misconception patterns among preservice teachers.

Despite these limitations, this pilot study provides preliminary insights into the persistence of astronomical misconceptions among preservice teachers across disciplines — a population underrepresented in the existing literature. The findings should be interpreted as exploratory rather than definitive, and future research with larger, multi-institutional samples is recommended to validate these patterns.

Thus, astronomical misconceptions persist among preservice teachers across disciplines, but why do these beliefs prove so resistant to formal instruction? The following section examines the cognitive and cultural mechanisms that sustain these myths.

Why myths persist

These empirical findings raise a critical question: why do astronomical misconceptions persist despite formal education? The answer lies in cognitive and cultural mechanisms that sustain these beliefs.

Research in cognitive development suggests that individuals begin constructing a 'naive framework theory of physics' during infancy based on their everyday observations (Driver 1989; Piaget 1929; Vosniadou 1994). These early-formed intuitions often persist into adulthood, resisting modification even through formal scientific instruction.

The persistence of these myths can be attributed to several key factors.

a) The formation of 'synthetic models'. When students encounter scientific facts that contradict their framework theories (e. g., 'the Earth is a sphere'), they often attempt to reconcile the two views rather than abandoning their initial beliefs. This leads to the creation of hybrid or synthetic models, such as the 'hollow Earth' model, where people are imagined to live on a flat surface inside a spherical shell to avoid falling 'down'.

b) Phenomenological primitives. Students often rely on simplified cognitive scripts known as p-prims, which are superficial interpretations of reality. A primary example is the 'closer means stronger' p-prim; this intuitive 'common sense' leads many to conclude that the Earth is hotter in the summer because it is closer to the Sun, ignoring the role of axial tilt (Comins 1998; 2001).

c) Influence of media and science fiction. Popular culture is a major external source of astronomical errors. Cartoons often portray physically implausible events that damage students' intuitions. Similarly, science fiction movies and TV-series, for example, frequently depict the asteroid belt as a densely packed region requiring complex maneuvering, whereas in reality, asteroids are separated by millions of kilometers.

d) Vernacular misconceptions. These arise from the use of words that have one meaning in everyday language and another in a scientific context (e. g., the words 'work', 'weight', 'energy', etc.). This, for instance, leads to difficulties in understanding scientific terms such as 'shooting star' (used for meteors) or the 'dark side of the Moon' (which implies it is never illuminated).

e) Personal cosmology and sensory misinterpretation. Most people develop a 'personal cosmology' to explain the origins and motions of the universe (Comins 1998; Piaget 1929). Since our senses prefilter information (for instance, the Sun appears yellow and seems to orbit a flat Earth), these uncritical interpretations are accepted as facts. Once a belief is incorporated into one's world view, individuals will go to extraordinary lengths to distort new facts to fit their existing beliefs.

In summary, astronomical myths are not simply a lack of knowledge but are coherent, internally consistent systems of explanation. Overcoming them requires more than just 'giving the right answer'; it requires the development of metaconceptual awareness, where learners begin to treat their beliefs as falsifiable hypotheses rather than unquestionable truths.

These cognitive and cultural factors explain why astronomical misconceptions prove resistant to traditional instruction. To translate this understanding into practice, educators need a structured tool to map specific misconceptions to observable phenomena. The following section presents such an object-based classification.

Object-based classification of astronomical misconceptions

Our classification of astronomical misconceptions integrates findings from academic literature, Millar's lists of students' misconceptions in physics (can be found at iop.org), and public science communication sources including blogs, podcasts, and documentaries. This synthesis reveals persistent patterns of misunderstanding that arise from the interplay between naive realism, gaps in physical knowledge, and cultural inertia.

We organize these misconceptions according to specific celestial objects — Stars and Constellations, the Moon, the Solar System, and the Sun — rather than abstract themes. This object-based approach was selected for its pedagogical alignment with standard astronomy curricula, its reflection of how learners cognitively structure celestial phenomena, and its capacity to address culturally specific myths associated with particular astronomical bodies.

Unlike previous topic-based classifications such as Comins', our framework grounds misconceptions in observable celestial objects, thereby facilitating more targeted educational interventions.

This classification framework focuses on observable celestial objects covered in standard school curricula. Misconceptions about specialized astrophysical objects (e. g., black holes, neutron stars) were intentionally excluded, as these topics are typically addressed at advanced levels. Future research may extend this framework to include such concepts.

Stars and Constellations

Misconceptions in this category are often driven by 'naive realism', where the sky is perceived as a solid dome and stars as burning points on a flat surface. Key errors include the following:

a) Physical nature. Stars are misunderstood as burning objects (ignoring thermonuclear fusion) or as 'falling' during meteor showers.

 https://www.doi.org/10.33910/2687-153X-2026-7-2-92-100

b) Spatial geometry. Constellations are incorrectly viewed as real, physical 3D groupings rather than arbitrary 2D regions of the sky.

c) Astrological influence. A persistent belief that celestial configurations mystically influence human destiny, supported by cognitive biases like the Barnum–Forer effect and the search for patterns in random data (apophenia).

We see the causes of these misconceptions in the historical roots of the animistic view of the sky, the persistence of naive realism, and the lack of understanding of stellar physics.

The Moon

Lunar myths are categorized by their perceived impact on human life and history.

a) Influence on behavior and health. The belief that full moons trigger insomnia, crime, or psychiatric disorders, often misapplying the Moon's gravitational effect on tides to the water in the human body.

b) Conspiracy theories. The 'Moon Hoax' myth, claiming the Apollo landings were fabricated. This arises from a misunderstanding of lunar physical conditions (e. g., shadows and lack of atmosphere) and a postmodern distrust of government institutions.

c) Everyday superstitions. Domestic myths where lunar phases are thought to dictate the timing of haircuts, agricultural work, or major life decisions.

Among the key causes of these misconceptions are illusory correlations, the influence of expectation effects, and insufficient understanding of gravitational physics.

The Solar System

This category covers misconceptions about planetary mechanics and characteristics.

a) The 'Planet Parade.' Alignments are misinterpreted as physical straight lines that exert catastrophic gravitational forces on Earth rather than simple optical phenomena.

b) The inner planets. Common errors include believing Mercury is the hottest planet due to its proximity to the Sun (in reality, Mercury's negligible atmosphere cannot retain heat, leading to extreme temperature fluctuations) and perceiving the asteroid belt as a dense, impassable field of rocks rather than a mostly empty space.

c) The outer planets. Jupiter is often mislabeled as a 'failed star', and Saturn's rings are incorrectly imagined as solid, monolithic disks.

d) Exoplanets and life. An anthropocentric bias that leads to the belief that habitable planets must be identical 'second Earths' and that life only exists in complex, intelligent forms.

We can attribute these misconceptions to the following factors: flawed extrapolation techniques; over-reliance on analogical thinking; the shaping effect of media imagery on public perception.

The Sun

Misconceptions about our star involve its physical nature and interaction with Earth.

a) Physical nature and the Sun's motion. Relics of geocentric thinking still suggest the Sun 'rises' or rotates around Earth. Its heat is often wrongly attributed to literal fire rather than plasma processes.

b) Influence on health and tech. The belief in a direct, deterministic link between every 'magnetic storm' and individual physical ailments (like headaches), as well as the myth that tanning is 'unconditionally healthy' while ignoring the risks of UV radiation.

These misconceptions stem from everyday sensory experience, false analogies, and ingrained linguistic patterns. The persistence of these barriers is driven not just by missing facts, but by imprecise language (like calling the Sun 'burning') and cognitive biases favoring simple explanations over scientific complexity.

This classification framework provides educators with a structured tool to map specific misconceptions to observable celestial objects. However, identifying misconceptions is only the first step. The following section outlines evidence-based pedagogical strategies for addressing each category within teacher training programs.

Implications for teacher training

Astronomy presents unique pedagogical challenges due to the nature of its subject matter. The phenomena it studies are typically inaccessible to direct experimentation, requiring instead prolonged observation of a megaworld where space and time are fundamentally interconnected. Astronomical

processes occurring on timescales are either too slow or too rapid for immediate perception, further complicated by the specific wavelengths at which these phenomena manifest (Zhukov et al. 1997).

To effectively address these pedagogical challenges, teacher training in modern science concepts — particularly astronomy — must transcend traditional fact-based instruction. Merely presenting accurate information fails to dislodge deeply held naive models; instead, students frequently merge new scientific facts with preexisting misconceptions, creating hybridized understandings (e. g., a disk-shaped Earth model). True conceptual transformation requires integrating the following instructional strategies into teacher preparation programs.

The five strategies outlined below correspond to the misconception categories from Section 3. For instance, 3D modeling addresses spatial geometry errors (Section 3.1b, 3.3), while 'what if?' questions challenge causal misconceptions about lunar and solar influence (Section 3.2a, 3.4b).

a) Development of pedagogical content knowledge. Effective teaching requires more than just subject matter knowledge; teachers must possess an in-depth understanding of how students represent abstract ideas that do not resonate with their daily experience (Loyola, Vanegas-Ortega 2021; Parker, Heywood 1998). A key measure of Pedagogical Content Knowledge is a teacher's ability to identify the most popular 'distractors' or wrong answers, which allows them to address entrenched misconceptions directly rather than assuming students are 'blank slates' (Sadler et al. 2009). By understanding the specific origins of myths — such as media influence, language imprecision, or 'common sense' p-prims — teachers can help students think more critically (Comins 1998).

b) Practical 3D modeling. A major barrier is the difficulty of translating 2D textbook diagrams into 3D relative motions (Parker, Heywood 1998; Zhukov et al. 1997). Practical modeling, such as using polystyrene spheres and torches to simulate the Earth–Moon–Sun system, is paramount for learners to clarify and articulate their ideas (Baxter 1989; Parker, Heywood 1998). Such hands-on discovery makes the invalidity of naive beliefs visible in a way that lectures cannot.

c) Predictive 'what if?' questions. Teachers should utilize 'what if?' scenarios to follow misconceptions to their logical (and often absurd) contradictions (Comins 1998). For instance, asking what would happen to the Earth's orbit if its mass changed helps students realize that mass does not affect orbital motion, proving their intuitive 'heavier means faster' models incorrect (Comins 2001).

d) Peer discussion and verbalization. Encouraging students to share their explanations and defend them against criticism helps them compare personal models with scientific ones (Baxter 1989; Vosniadou 1994). Peer-led discussions transform the classroom from passive listening to active engagement, which has been shown to help even students with weaker backgrounds perform significantly better (Baxter 1989; Parker, Heywood 1998).

e) Historical parallels. Referring to historical ideas, such as the geocentric system, can make students feel more comfortable by showing that their naive notions were once the accepted scientific view (Baxter 1989). This highlights the tentative nature of science and the types of evidence required to change a theory.

Together, these strategies provide a practical toolkit for addressing the specific misconception categories identified in this study. Implementation within teacher training programs can help future educators recognize and correct these persistent errors in their own understanding before entering the classroom.

Conclusion

The documented cases of astronomical misconceptions among preservice teachers in our sample illustrate a potential gap in teacher training. Further research is needed to determine the prevalence of these patterns. Existing literature suggests that high academic achievement does not automatically eliminate naive framework theories established in childhood.

The categorization of misconceptions provided in our study is a vital tool for the development of Pedagogical Content Knowledge. Teacher education must focus on the processes of conceptual acquisition, making teachers explicitly aware of the specific misconceptions they will encounter in the classroom.

Future research with larger, multi-institutional samples is recommended to validate the proposed classification framework and test the effectiveness of the pedagogical strategies outlined herein.

Ultimately, the goal of physics education is to foster a 'metaconceptual awareness' that allows learners to distinguish between appearance and reality (Vosniadou 1994). By directly addressing the roots of incorrect beliefs — such as the confusion between the solar system and the galaxy or the 'no gravity in space' myth — educators can help students move toward a coherent, scientific worldview.

 https://www.doi.org/10.33910/2687-153X-2026-7-2-92-100

Overcoming these misconceptions is the first step in freeing the mind, allowing individuals to understand how the natural world truly operates and to use that knowledge to make informed decisions.

A final thought

One respondent captured this nuanced relationship with astrology: '*I consider astrology a tool for self-reflection. People want to feel special, with unique characteristics. When we read a horoscope, we note traits that resemble us and criticize what doesn't apply. I don't believe in predictions, but I know my friends' zodiac signs. It's simply a curious way to learn more about yourself*'. (B.Ed. 1st-year student, Psychology)

This perspective serves as one example of how astrology can occupy a space between belief and curiosity — a psychological tool rather than a scientific claim. Understanding this distinction is essential for educators seeking to foster scientific literacy without dismissing the human need for meaning and self-understanding.

Conflict of Interest

The authors declare that there is no conflict of interest, either existing or potential.

Author Contributions

All authors contributed equally to this work. A. N. Krushelnitckii: conceptualization, theoretical framework, methodology supervision, manuscript writing, and final approval. T. D. Razboinikova: survey design, data collection and analysis, development of the object-based misconception classification. A. I. Kolesnikova: literature review, manuscript editing and formatting.

Acknowledgements

The authors express their gratitude to Professor Vladimir Pronin (Department of Theoretical Physics and Astronomy, Herzen University) for his support.

References

Baxter, J. (1989) Children's understanding of familiar astronomical events. *International Journal of Science Education*, 11 (5), 502–513. https://doi.org/10.1080/0950069890110503 (In English)

Comins, N. F. (1998) Identifying and addressing astronomy misconceptions in the classroom. *International Astronomical Union Colloquium*, 162, 118–123. https://doi.org/10.1017/S0252921100114927 (In English)

Comins, N. F. (2001) *Heavenly errors: Misconceptions about the real nature of the Universe*. New York: Columbia University Press, 244 p. (In English)

Driver, R. (1989) Students' conceptions and the learning of science. *International Journal of Science Education*, 11 (5), 481–490. https://doi.org/10.1080/0950069890110501 (In English)

Hennig, F., Lipps, M., Ubben, M. S., Bitzenbauer, P. (2023) From the Big Bang to life beyond Earth: German preservice physics teachers' conceptions of astronomy and the nature of science. *Education Sciences*, 13 (5), article 475. https://doi.org/10.3390/EDUCSCI13050475 (In English)

Krushelnitckii, A., Razboinikova, T. (2026) Survey instrument: Astronomical misconceptions among preservice teachers. *Zenodo*. [Online] Available at: https://doi.org/10.5281/zenodo.19055075 (accessed 18.03.2026). (In English)

Loyola, F. R., Vanegas-Ortega, C. (2021) Concepciones alternativas sobre astronomía en estudiantes de educación básica y media de la Región Metropolitana de Chile [Alternative conceptions of astronomy in students of basic and high school in the Metropolitan Region of Chile]. *Estudios pedagógicos (Valdivia)*, 47 (2), 247–268. https://doi.org/10.4067/S0718-07052021000200247 (In Spanish)

Nandi, K. K., Akhtaryanova, G. F., Izmailov, R. N. (2015) Astronomical literacy as an integral part of the scientific worldview of the student. *Pedagogical Journal of Bashkortostan*, 3 (58), 41–47. (In Russian)

Parker, J., Heywood, D. (1998) The earth and beyond: Developing primary teachers' understanding of basic astronomical events. *International Journal of Science Education*, 20 (5), 503–520. https://doi.org/10.1080/0950069980200501 (In English)

Piaget, J. (1929) *The child's conception of the world*. London: Routledge & K. Paul Publ., 397 p. (In English)

Rajpaul, V., Allie, S., Blyth, S.-L. (2014) Introductory astronomy course at the University of Cape Town: Probing student perspectives. *Physical Review Special Topics — Physics Education Research*, 10 (2), article 020126. https://doi.org/10.1103/PHYSREVSTPER.10.020126 (In English)

Sadler, P. M., Coyle, H., Miller, J. L. et al. (2009) The astronomy and space science concept inventory: Development and validation of assessment instruments aligned with the K-12 National Science Standards. *Astronomy Education Review*, 8 (1), article 010111. https://doi.org/10.3847/AER2009024 (In English)

Vosniadou, S. (1994) Capturing and modeling the process of conceptual change. *Learning and Instruction*, 4 (1), 45–69. https://doi.org/10.1016/0959-4752(94)90018-3

Zhukov, L. V. (2021) *Explanatory dictionary of astronomy*. Saint Petersburg: Herzen State Pedagogical University of Russia Publ., 690 p. (In Russian)

Zhukov, L. V., Pronin, V. P., Sokolova, I. I. (1997) Undergraduate research using computers as a form of preparing physics and astronomy teachers. *Physics in Higher Education*, 3 (4), 124–127. (In Russian)

Summaries in Russian / Информация о статьях на русском языке

Физика конденсированного состояния

КОРРЕЛЯЦИИ МЕЖДУ ДАННЫМИ ЯМР, ДАННЫМИ МЁССБАУЭРОВСКОЙ СПЕКТРОСКОПИИ И ПАРАМЕТРАМИ ТЕНЗОРА ГРАДИЕНТА ЭЛЕКТРИЧЕСКОГО ПОЛЯ ДЛЯ МЕДНЫХ УЗЛОВ В СВЕРХПРОВОДЯЩИХ ОКСИДАХ МЕТАЛЛОВ $RBa_2Cu_3O_{7-x}$

Алла Валентиновна Марченко, Тамара Эргашбаевна Баймирзаева, Валентин Сергеевич Киселев, Павел Павлович Серегин

Аннотация. Были определены линейные отношения между константами квадрупольного взаимодействия, измеренными методом ядерного магнитного резонанса с изотопом ^{63}Cu, методом эмиссионной мёссбауэровской спектроскопии с изотопом ^{67}Zn, и главной компонентой тензора градиента электрического поля в медных узлах керамических сверхпроводников $RBa_2Cu_3O_7$. Эти отношения позволяют, без использования каких-либо моделей распределения заряда по узлам в кристаллической решетке, определять соединения, в которых медь является двухвалентной.

Ключевые слова: ядерный магнитный резонанс, мёссбауэровская спектроскопия, тензор градиента электрического поля, высокотемпературные сверхпроводники, электронные дефекты

Для цитирования: Marchenko, A. V., Baimirzaeva, T. E., Kiselev, V. S., Seregin, P. P. (2026) Correlations between NMR data, Mössbauer spectroscopy data and the EFG tensor parameters for copper nodes in $RBa_2Cu_3O_{7-x}$ superconducting metal oxides. *Physics of Complex Systems*, 7 (2), 59–64. https://www.doi.org/10.33910/2687-153X-2026-7-2-59-64 EDN CGGAPH

ИМПРИНТ В СФЕРОЛИТОВЫХ ТОНКИХ ПЛЕНКАХ ЦИРКОНАТА-ТИТАНАТА СВИНЦА

Владимир Петрович Пронин, Артемий Николаевич Крушельницкий, Алсу Равилевна Мазгутова, Евгений Юрьевич Каптелов, Станислав Викторович Сенкевич, Игорь Петрович Пронин, Сергей Александрович Немов

Аннотация. Исследуется влияние микроструктуры (геометрических размеров сферолитовых блоков), амплитуды внешнего поля и старения на величину внутреннего поля (импринта) в тонких пленках цирконата-титаната свинца, сформированных двухстадийным методом ВЧ магнетронного распыления на платинированной подложке кремния. Показано, что увеличение внутреннего поля в процессе старения происходит в результате восходящей диффузии кислородных вакансий (эффекта Горского), вызванной изгибными механическими напряжениями в тонкой пленке. Предполагается, что источником кислородных вакансий в перовскитовой решетке служит доокисление избыточного оксида свинца, расположенного на интерфейсах и в межкристаллитном пространстве тонких пленок.

Ключевые слова: тонкие пленки ЦТС, ВЧ магнетронное распыление, сферолитовая микроструктура, импринт, самополяризация, кислородные вакансии

Для цитирования: Pronin, V. P., Krushelnitckii, A. N., Mazgutova, A. R., Kaptelov, E. Yu., Senkevich, V. S., Pronin, I. P., Nemov, S. A. (2026) Imprint in spherulitic thin films of lead zirconate titanate. *Physics of Complex Systems*, 7 (2), 65–73. https://www.doi.org/10.33910/2687-153X-2026-7-2-65-73 EDN JCWNAV

ВЛИЯНИЕ УФ НА ПРОЦЕССЫ ЭЛЕКТРИЧЕСКОЙ РЕЛАКСАЦИИ В ОБЛАСТИ ТЕМПЕРАТУРЫ СТЕКЛОВАНИЯ ПЭТФ

Иван Алексеевич Федоров, Анастасия Валентиновна Степченкова, Никита Петрович Бебенин, Елена Алексеевна Волгина, Дмитрий Эдуардович Темнов

Аннотация. Методом термоактивационной спектроскопии исследовались процессы электрической релаксации, наблюдаемые в полиэтилентерефталате. В области температуры стеклования данного полимера обнаружено два релаксационных процесса — в области 60°C и 80°C. Относительная интенсивность этих процессов существенно изменялась после УФ-облучения полимера.

Показано, что релаксация в области 60°C связана с процессом стеклования, развивающимся в аморфной фазе полимера. Релаксация в области 80°C может быть связана с частью аморфной фазы у поверхности кристаллитов (rigid amorphous fraction), характеризующейся пониженной подвижностью молекулярных сегментов. После УФ-облучения данного полимера относительное содержание этой фракции существенно возрастает.

Ключевые слова: полиэтилентерефталат, термостимулированная деполяризация, температура стеклования, УФ-излучение, электрическая релаксация

Для цитирования: Fedorov, I. A., Bebenin, N. P., Stepchenkova, A. V., Volgina, E. A., Temnov, D. E. (2026) The influence of ultraviolet radiation on electrical relaxation processes within the temperature area of stained glass films of PET. *Physics of Complex Systems*, 7 (2), 74–78. https://www.doi.org/10.33910/2687-153X-2026-7-2-74-78 EDN JDXSII

Физика полупроводников

ЭЛЕКТРОФИЗИЧЕСКИЕ СВОЙСТВА НАНОКОМПОЗИТА СЕГНЕТОВА СОЛЬ / ЦЕОЛИТ А (ЧАСТЬ 2)

Тамара Геннадьевна Матвеева, Рене Алехандро Кастро Арата, Владимир Гаевич Соловьев

Аннотация. В диапазоне частот от 0.1 Гц до 1 МГц при нагревании от 273 до 493 К были исследованы электропроводность, диэлектрическая проницаемость и диэлектрические потери нанокомпозита, полученного путем пропитки матрицы-«хозяина» цеолита NaA веществом-«гостем», в качестве которого выступала сегнетова соль (калий-натрий виннокислый 4-водный, или двойной калий-натриевый тартрат $KNaC_4H_4O_6{\times}4H_2O$). Обсуждаются характерные особенности частотных и температурных зависимостей электрофизических характеристик нанокомпозита сегнетова соль / цеолит А.

Ключевые слова: сегнетоэлектрики, сегнетова соль, диэлектрическая проницаемость, диэлектрические потери, электропроводность, цеолит, нанокомпозит

Для цитирования: Matveeva, T. G., Castro Arata, R. A., Solovyev, V. G. (2026) Electrophysical properties of the Rochelle salt / zeolite A nanocomposite (Part 2). *Physics of Complex Systems*, 7 (2), 79–83. https://www.doi.org/10.33910/2687-153X-2026-7-2-79-83 EDN SKNMEI

Теоретическая физика

ЯДЕРНОЕ МАГНИТНОЕ ЭКРАНИРОВАНИЕ И КВАДРАТИЧНЫЙ ЭФФЕКТ ЗЕЕМАНА В ИОНАХ, ПОДОБНЫХ ГЕЛИЮ

Валентин Александрович Агабабаев, Дмитрий Алексеевич Глазов, Матвей Максимович Осипцов, Андрей Викторович Волотка, Владимир Моисеевич Шабаев

Аннотация. Квадратичный эффект Зеемана и сверхтонкое магнитное экранирование рассчитаны в гелиеподобных ионах в основном $(1s)^2$ состоянии с помощью теории возмущений. Численные значения получены для диапазона зарядов ядра $Z = 6 – 32$. Зеемановское расщепление оценивается путем решения уравнения Дирака в кулоновском поле с конечным ядром с использованием B-сплайнов, построенных в рамках метода ДКБ. Вклады ведущего порядка, а также однофотонные обменные поправки рассматриваются в рамках строгого подхода КЭД. Рассчитанные константы ядерного магнитного экранирования могут быть использованы для определения ядерных магнитных моментов, в то время как квадратичный эффект Зеемана имеет значение для прецизионных измерений энергий переходов в гелиеподобных ионах в ловушках Пеннинга.

Ключевые слова: эффект Зеемана, g-фактор, многозарядные ионы, КЭД связанных состояний, ядерное магнитное экранирование, сверхтонкая структура

Для цитирования: Agababaev, V. A., Glazov, D. A., Osiptsov, M. M., Volotka, A. V., Shabaev, V. M. (2026) Nuclear magnetic shielding and quadratic Zeeman effect in helium-like ions. *Physics of Complex Systems*, 7 (2), 84–91. https://www.doi.org/10.33910/2687-153X-2026-7-2-84-91 EDN ZTCZJC

Проблемы физического образования

МЕЖДУ АСТРОНОМИЕЙ И АСТРОЛОГИЕЙ: ЗАБЛУЖДЕНИЯ БУДУЩИХ УЧИТЕЛЕЙ О НЕБЕСНЫХ ОБЪЕКТАХ

Артемий Николаевич Крушельницкий, Татьяна Дмитриевна Разбойникова, Анна Игоревна Колесникова

Аннотация. В статье рассматривается проблема устойчивости астрономических заблуждений у будущих педагогов. Исследование вносит два вклада: 1) предложена объектно ориентированная классификация заблуждений (звезды и созвездия, Луна, Солнечная система, Солнце), основанная на когнитивной теории и согласованная со школьными программами; 2) проиллюстрирована распространенность заблуждений через данные пилотного опроса 69 студентов одного российского педагогического вуза. Опросник не является валидированным инструментом и служит для демонстрации прецедента, а не измерения популяционной распространённости. Результаты показывают, что 68,1% респондентов путают зодиакальные знаки и астрономические созвездия, 42% согласны с идеей астрологии как «ворот» в астрономию. Обсуждаются когнитивные механизмы устойчивости мифов (наивные теории, синтетические модели, p-prims) и пять педагогических стратегий для работы с заблуждениями при подготовке учителей.

Ключевые слова: астрономические заблуждения, астрология, подготовка учителей, педагогические стратегии, научная грамотность, классификация заблуждений, когнитивные механизмы

Для цитирования: Krushelnitckii, A. N., Razboinikova, T. D., Kolesnikova, A. I. (2026) Between astronomy and astrology: Preservice teachers' misconceptions about celestial objects. *Physics of Complex Systems*, 7 (2), 92–100. https://www.doi.org/10.33910/2687-153X-2026-7-2-92-100 EDN XLKEIV